Characterization of Tajogaite volcanic plumes detected over the Iberian Peninsula from a set of satellite and ground-based remote sensing instrumentation

V. Salgueiro, J.L. Guerrero-Rascado, M.J. Costa, R. Román, A. Cazorla, A. Serrano, F. Molero, Michaël Sicard, C. Córdoba-Jabonero, D. Bortoli, et al.

Remote Sensing of Environment 295 (2023) 113684

Contents lists available at ScienceDirect

Remote Sensing of Environment

journal homepage: www.elsevier.com/locate/rse

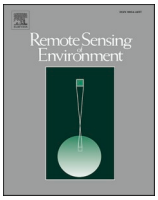

Characterization of Tajogaite volcanic plumes detected over the Iberian Peninsula from a set of satellite and ground-based remote sensing instrumentation

V. Salgueiro [a,b,*], J.L. Guerrero-Rascado [c,d], M.J. Costa [a,b], R. Román [e], A. Cazorla [c,d], A. Serrano [f], F. Molero [g], M. Sicard [h,i], C. Córdoba-Jabonero [j], D. Bortoli [a,b], A. Comerón [h], F.T. Couto [a,b], M.Á. López-Cayuela [j], D. Pérez-Ramírez [c,d], M. Potes [a,b], J.A. Muñiz-Rosado [c,d], M.A. Obregón [f], R. Barragán [g], D.C.F.S. Oliveira [h], J. Abril-Gago [c,d], R. González [e], C. Gíl-Díaz [h], I. Foyo-Moreno [c,d], C. Muñoz-Porcar [h], M.J. Granados-Muñoz [c,d], A. Rodríguez-Gómez [h], M. Herreras-Giralda [k], J.A. Bravo-Aranda [c,d], C.V. Carvajal-Pérez [j], A. Barreto [l], L. Alados-Arboledas [c,d]

[a] Earth Remote Sensing Laboratory (EaRSLab), University of Évora, Évora 7000-671, Portugal
[b] Institute of Earth Sciences (ICT) and Department of Physics, Institute for Advanced Studies and Research (IIFA) and School of Sciences and Tecnology (ECT), University of Évora, Évora 7000-671, Portugal
[c] Andalusian Institute for Earth System Research, Granada 18006, Spain
[d] Applied Physics Department, University of Granada, 18071, Spain
[e] Group of Atmospheric Optics (GOA-UVa), University of Valladolid, Valladolid 47011, Spain
[f] Departmento de Física, Universidad de Extremadura, Badajoz 06006, Spain
[g] Centre for Environmental and Technological Energy research (CIEMAT), Madrid 28040, Spain
[h] CommSensLab, Department of Signal and Theory and Communications, Universitat Politècnica de Catalunya (UPC), Barcelona 08034, Spain
[i] Laboratoire de l'Atmosphère et des Cyclones (LACy), Université de la Réunion, Saint-Denis 97744, France
[j] Atmospheric Research and Instrumentation Branch, Instituto Nacional de Técnica Aeroespacial (INTA), Torrejón de Ardoz, Madrid 28850, Spain
[k] Lab. d'Optique Atmos., CNRS, Lille 1 University and GRASP-SAS, Villeneuve D'Ascq, France
[l] Izaña Atmospheric Research Center, Meteorological State Agency of Spain (AEMET), Izaña, Spain

ARTICLE INFO

Edited by Menghua Wang

Keywords:
Sulphur dioxide
Volcanic sulphates
GRASP algorithm
Lidar
Ceilometer
Sun-photometer
Satellite remote sensing

ABSTRACT

Three volcanic plumes were detected during the Tajogaite volcano eruptive activity (Canary Islands, Spain, September–December 2021) over the Iberian Peninsula. The spatiotemporal evolution of these events is characterised by combining passive satellite remote sensing and ground-based lidar and sun-photometer systems. The inversion algorithm GRASP is used with a suite of ground-based remote sensing instruments such as lidar/ceilometer and sun-photometer from eight sites at different locations throughout the Iberian Peninsula. Satellite observations showed that the volcanic ash plumes remained nearby the Canary Islands covering a mean area of 120 ± 202 km^2 during the whole period of eruptive activity and that sulphur dioxide plumes reached the Iberian Peninsula. Remote sensing observations showed that the three events were mainly composed of sulphates, which were transported from the volcano into the free troposphere. The high backscatter-related Ångström exponents for wavelengths 532–1064 nm (1.17 ± 0.20 to 1.40 ± 0.24) and low particle depolarization ratios (0.08 ± 0.02 to 0.09 ± 0.02), measured by the multi-wavelength Raman lidar, hinted at the presence of spherical small particles. The layer aerosol optical depth at 532 nm (AOD_L^{532}) obtained from lidar measurements contributed between 49% and 82% to the AERONET total column AOD at 532 nm in event II (11–13 October). According to the GRASP retrievals, the layer aerosol optical depth at 440 nm (AOD_L^{440}) was higher in all sites during event II with values between 0.097 (Badajoz) and 0.233 (Guadiana-UGR) and lower in event III (19–21 October) varying between 0.003 (Granada) and 0.026 (Évora). Compared with the GRASP retrievals of total column AOD at 440 nm, the AOD_L^{440} had contributions between 21% and 52% during event II. In the event I (25–28 September), the mean volume concentrations (VC) varied between 5 ± 4 μm^{3}cm^{-3} (El-Arenosillo/Huelva) and 17 ± 10 μm^{3}cm^{-3}

* Corresponding author.
E-mail address: vsalgueiro@uevora.pt (V. Salgueiro).

https://doi.org/10.1016/j.rse.2023.113684
Received 13 October 2022; Received in revised form 26 April 2023; Accepted 8 June 2023
Available online 13 June 2023

(Guadiana-UGR), while in event II this variation was from 11 ± 7 $\mu m^3 cm^{-3}$ (Badajoz) to 27 ± 10 $\mu m^3 cm^{-3}$ (Guadiana-UGR). Due to the impact of volcanic events on atmospheric and economic fields, such as radiative forcing and airspace security, a proper characterization is required. This work undertakes it using advanced instrumentation and methods.

1. Introduction

Volcanic eruptions are important natural sources of atmospheric compounds by injecting ash particles and gases, such as carbon dioxide (CO_2), water vapour (H_2O) and sulphur dioxide (SO_2), into the atmosphere (Robock, 2000). Depending on the volcano's explosivity and maximum height reached by the ejected volcanic materials (troposphere or stratosphere), volcanic aerosols may influence the climate by affecting the global radiative balance, surface temperatures (Minnis et al., 1993; Robock, 2000) and even tropospheric cloud formations (Gassó, 2008). The explosive Mount Pinatubo eruption in 1991 was an example of how volcanic events can impact the climate and temperature at the surface. This eruption injected enormous amounts of SO_2 that reached the stratosphere. Once in the stratosphere, the SO_2 converted into sulphate particles produced a radiative forcing of -2.7 ± 1.0 Wm^{-2} leading to a surface cooling effect (Minnis et al., 1993). Recently, in January 2022, the Hunga Tonga-Hunga Ha'apai volcano (a submarine volcano in the South Pacific Ocean) produced a large explosive event that injected unprecedented amounts of H_2O into the stratosphere (146 ± 5 Tg, i.e., ~10% of the stratospheric burden), which could impact climate through a surface warming due to the radiative forcing from the excess stratospheric H_2O (Millán et al., 2022). Besides the climate effects, volcano emissions also impact air quality and airspace security (e.g. Stewart et al., 2022) as in 2010, when several countries in Europe needed to close their airspace for some days due to the Eyjafjallajökull eruption (e.g., Colette et al., 2011; Sicard et al., 2012). Therefore, it is essential to monitor and study volcanic aerosols since they impact life on Earth.

The Tajogaite volcano is located in the Cumbre Vieja rift in La Palma Island (28.57°N, 17.83°W; volcanic edifice elevation of 1121 m asl), at the north-western end of the Canary Islands (Spain). Its latest eruption started on 19 September 2021 and lasted until 13 December 2021 (Instituto Geográfico Nacional, 2022). For three months, the volcanic eruption, of Strombolian type, produced lava fountains and flows, and injected ash and gases into the atmosphere. The eruption, characterised by a mixed mechanism of simultaneous explosive and effusive phases, was labelled with a volcanic explosivity index (VEI) of 3, an indicator of the explosive nature of an eruption (Newhall and Self, 1982), by the "*Plan Especial de Protección Civil y Atención de Emergencias por riesgo volcánico en la Comunidad Autónoma de Canarias*" (PEVOLCA, 2021), injecting volcanic aerosols a few kilometres up in the atmosphere with plumes detected as high as 5.5 km asl during the month of October (Global Volcanism Program, 2022). Active remote sensing observations in Tazacorte, around 10 km distance from the volcano, showed that daily mean peak heights of the lowermost volcanic plumes did not exceed 3 km asl and lofted layers with heights above 3 km asl were rare in the period from 15 October to the end of the volcanic eruptive activity (Sicard et al., 2022; Córdoba-Jabonero et al., 2023).

Concerning the importance of volcanic emissions on the climate system, over the past years several studies have been carried out to access the impact of volcanic eruptions in the atmosphere by using remote sensing instrumentation such as lidar systems (e.g., Ansmann et al., 2011; Córdoba-Jabonero et al., 2023; Hervo et al., 2012; Kokkalis et al., 2013; Lopes et al., 2019; Mattis et al., 2010; Mona et al., 2012; Navas-Guzmán et al., 2013; Papayannis et al., 2012; Prata et al., 2017; Sannino et al., 2022; Sawamura et al., 2012; Sicard et al., 2012, 2022). These systems allow for the detection and monitoring of aerosols, providing continuous measurements of high vertical and temporal resolutions at wavelengths suitable for aerosol profiling characterization. In addition to the lidar systems, ceilometers can measure the atmospheric backscattered signal up to 15 km (Cazorla et al., 2017) working continuously. The use of data from coordinated observation networks with standardized data processing procedures like the "European Aerosol Research Lidar Network" (EARLINET) (Pappalardo et al., 2014), the "NASA Micro-Pulse Lidar Network" (MPLNET) (Welton et al., 2001) and the "Iberian Ceilometer Network" (ICENET) (Cazorla et al., 2017), is fundamental to monitor the aerosol evolution in terms of their vertically-resolved properties on a large spatial scale. Besides, the synergy between the different remote sensing instrumentation and the application of algorithms to their measurements provide a comprehensive assessment of the aerosol properties. The "Generalized Retrieval of Aerosol and Surface Properties" (GRASP; www.grasp-open.com) (Dubovik et al., 2014, 2021) permits such combinations of measurements. For instance, GRASP allows retrieving columnar and vertically resolved aerosol properties such as volume concentration profiles using the combination of co-located AERONET sun-photometer measurements with range corrected signal from multi-wavelength lidar (Lopatin et al., 2013, 2021) or from single-wavelength lidars like ceilometer (Román et al., 2018). Many studies carried out over the Iberian Peninsula (IP) use these GRASP configurations, the combinations of the spectral AOD with multi-wavelength and single-wavelength lidar signals (Benavent-Oltra et al., 2017, 2019; López-Cayuela et al., 2021, 2022; Román et al., 2018), specifically to derive optical and microphysical properties of mineral dust (e.g., Benavent-Oltra et al., 2017, 2019; López-Cayuela et al., 2021), smoke (e.g., López-Cayuela et al., 2022) and aerosol temporal series observations over urban (e.g., Molero et al., 2020) and mountain (e.g., Herreras et al., 2019; Titos et al., 2019) sites.

Moreover, over the IP, volcanic aerosol (VA) plumes transported from the Eyjafjallajökull (Iceland, April–May 2010) and Nabro (Eritrea, June 2011) eruptions were observed and monitored (Navas-Guzmán et al., 2013; Sawamura et al., 2012; Sicard et al., 2012; Toledano et al., 2012) by using lidar measurements performed at different sites. More recently, the occurrence of the Tajogaite eruption and the transport of the volcanic plumes towards the IP provides an opportunity to study the evolution of volcanic aerosols transport in the troposphere. This work aims to characterise the spatiotemporal evolution of aerosol optical and microphysical properties of three VA events detected over the IP during the Tajogaite volcano eruptive activity from September to December 2021. These plumes resulted from different transport patterns that were monitored, among others, by the Copernicus Atmosphere Monitoring Service (CAMS) satellite observations of the SO_2 total vertical column, used as a proxy for the presence of VA (Sears et al., 2013). The aerosol characterization was performed through the use of a set of vertically resolved and columnar-integrated observations and the GRASP algorithm was applied to those measurements carried out at eight sites distributed over the IP and integrated into the different mentioned networks (EARLINET, ICENET and MPLNET).

The paper is organised as follows. Section 2 gives a description of the methods and data used for the VA characterization. In section 3 the results are presented and discussed, and in section 4 the conclusions are given.

2. Methods and data

2.1. Satellite data

The monitorization of volcanic ash plumes from space was done with the brightness temperature difference (BTD) method (Prata, 1989),

based on the increase of absorption by ashes in the range of 10–13 μm. To this aim, 1-km resolution calibrated radiances from MODIS/Aqua collection 6.1 level 1B data from NASA were used. Concretely, brightness temperature at 11 μm minus brightness temperature at 12 μm was retrieved from channels #32 (11.030 μm) and #31 (12.020 μm), respectively, using the SNAP (Sentinel Application Platform, https://step.esa.int/main/download/snap-download/) tool, developed by the European Space Agency (ESA). The method relies on identifying pixels affected by volcanic ash by the use of negative BTD (larger absorption at 11 than at 12 μm), after contextual filtering of false positives, which might be present over certain scenarios such as soils with high quartz content, ice-covered surfaces, high altitude clouds with low cloud-top temperatures and prevalence of clear sky situations with negligible atmospheric absorption (Picchiani et al., 2011; Prata and Prata, 2012; Watkin, 2003). Such a procedure has been successfully applied in previous studies such as Mt. Etna (Corradini et al., 2009, 2010), Mt. Cleveland (Kearney and Watson, 2009) and Eyjafjallajökull (Dubuisson et al., 2013), among others. Finally, the volcanic ash plume top height has been derived by comparing the ash plume top temperature, computed as the coldest brightness temperature of channel #32 of the most opaque plume region, and the temporal-spatial closest radio sounding temperature profile (Corradini et al., 2008). To this aim, 3-h GDAS ("Global Data Assimilation System"; https://www.ncei.noaa.gov/; last access on 24 September 2022) data were used.

The tropospheric SO_2 total vertical column density data from the Tropospheric Monitoring Instrument (TROPOMI) onboard Copernicus Sentinel-5 Precursor (Sentinel-5P) satellite (Veefkind et al., 2012) were used to detect and track the transport of the volcanic plumes over the IP. TROPOMI is a spectrometer that acquires data at four different spectral regions (ultraviolet, visible, near-infrared and shortwave infrared) providing, with a high spatial resolution of 7×7 km^2, daily global information on trace gases and aerosols, important for air quality monitoring and climate studies (Veefkind et al., 2012). The data used correspond to TROPOMI Level 2 SO_2 data product. These data were downloaded from the European Space Agency (ESA) Sentinel-5P Pre-Operations Data Hub (https://s5phub.copernicus.eu/; last access on 5 August 2022). The SO_2 total vertical column analysis was carried out by using the HARP toolkit (Python interface) of the Atmospheric Toolbox (available at https://atmospherictoolbox.org/; last accessed on 5 August 2022). The SO_2 data (mol·m^{-2}) was converted to DU (1 DU = 2.69×10^{16} molecules·cm^{-2}) and only pixels with a quality value above 0.5 were considered according to the recommendations of the data usage documentation (Sentinel, 2021).

2.2. Meteorological data and backwards-trajectories

The synoptic conditions that favoured the advection of the volcanic plumes to the IP are described by using the ERA5 reanalysis of the European Centre for Medium-Range Weather Forecasts (ECMWF) (https://cds.climate.copernicus.eu/; last accessed on June 30, 2022). The atmospheric flow is analysed by means of wind speed and direction at 700 hPa pressure level, i.e., approximately 3 km altitude, according to the mean peak heights of the lowermost volcanic plumes reported by Sicard et al. (2022). The origin of the aerosols is checked with HYSPLIT (Hybrid Single Particle Lagrangian Integrated Trajectory Model) (Stein et al., 2015) backward trajectories. To this end, the 144 h (6-day) backward trajectories were calculated starting at the different site locations for altitudes between 1 and 5 km above ground level with steps of 0.5 km and with time steps of 60 min.

2.3. Ground-based remote sensing: Measurement sites and instrumentation

Aerosol observations were performed at eight sites distributed over the IP, all equipped with remote sensing instrumentation for aerosol observations (Table 1). All the sites are equipped with CIMEL sun-photometers integrated into AERONET (Holben et al., 1998). The Évora site is equipped with the Portable Aerosol and clOud LIdar (PAOLI), a multiwavelength Raman lidar PollyXT system (Althausen et al., 2009). The Raman lidar system is part of the EARLINET (Pappalardo et al., 2014) in the frame of Aerosols, Clouds and Trace Gases Research Infrastructure Network (ACTRIS). El-Arenosillo/Huelva and Barcelona sites are both equipped with polarized Micro-Pulse Lidar (MPL) systems operating within MPLNET (Welton et al., 2001). Granada, Guadiana-UGR, Badajoz and Madrid are equipped with Lufft CHM15k-Nimbus ceilometers integrated into ICENET (Cazorla et al., 2017).

Table 1
Description of the eight stations and the respective instrumentation used in this work.

Site	Location	Research centre	Instrumentation
Barcelona, Spain (BCN)	41.39°N, 2.11°E, 125 m asl	Polytechnic University of Catalonia (UPC)	Polarized Micro-Pulse Lidar, CIMEL CE-318-TP9 sun-sky-moon photometer
Madrid, Spain (MDR)	40.45°N, 3.72°W, 680 m asl	Centre for Environmental and Technological Energy Research (CIEMAT)	Lufft Nimbus-15 k ceilometer, CIMEL CE-318-4 sun-sky photometer
Badajoz, Spain (UEX)	38.88°N, 7.01°W, 199 m asl.	University of Extremadura	Lufft Nimbus-15 k ceilometer, CIMEL CE-318 sun-sky photometer
Évora, Portugal (EVO)	38.57°N, 7.91°W, 293 m asl	Institute of Earth Sciences (ICT), University of Évora	Multiwavelength Raman Lidar, CIMEL CE-318-2 sun-sky-moon photometer
Guadiana-UGR, Spain (GDN)	37.91°N, 3.23°W, 370 m asl	Andalusian Institute for Earth System Research (IISTA-CEAMA), University of Granada	Lufft Nimbus-15 k ceilometer, CIMEL CE-318 sun-sky photometer
Granada, Spain (UGR)	37.16°N, 3.61°W, 680 m asl	Andalusian Institute for Earth System Research (IISTA-CEAMA), University of Granada	Lufft Nimbus-15 k ceilometer, CIMEL CE-318 sun-sky photometer
Cerro Poyos, Spain (UGR^{CP})	37.11°N, 3.49°W, 1830 m asl	Andalusian Institute for Earth System Research (IISTA-CEAMA), University of Granada	CIMEL CE-318 sun-sky photometer
El-Arenosillo/ Huelva, Spain (ARN)	37.11°N, 6.73°W, 59 m asl	Spanish Institute for Aerospace Technology (INTA)	Polarized Micro-Pulse Lidar, CIMEL CE-318 sun-sky-moon photometer

2.3.1. Multi-wavelength Raman lidar

A multi-wavelength Raman lidar system PAOLI, with three elastic channels (355, 532 and 1064 nm), two inelastic channels (387 and 607 nm) and one cross-polarization channel (532 nm) is installed at Évora (EVO) site. It supplied continuous vertical profile measurements of backscatter and extinction coefficients, as well as particle linear depolarization, with vertical and temporal resolutions of 30 m and 30 s, respectively (Salgueiro et al., 2021). The overlap of this lidar system roughly affects heights below 800 m; other technical details of this lidar can be found in the literature (Preißler et al., 2011). The EARLINET's Single Calculus Chain (SCC) (D'Amico et al., 2016; Mattis et al., 2016) was used to retrieve the profiles of the optical variables. During daytime, only the elastic lidar signals were used due to the strong radiation background (Althausen et al., 2009) and the Klett-Fernald method (Fernald et al., 1972; Fernald, 1984; Klett, 1981, 1985) was applied considering a fixed lidar ratio of 50 ± 15 sr (e.g., Sicard et al., 2012; López-Cayuela et al., 2023) to calculate particle backscatter coefficient profiles. At night, the inelastic lidar signals were used to obtain independent particle backscatter and extinction coefficient profiles using the Raman method (Ansmann et al., 1992). The particle linear

depolarization ratio at 532 nm is retrieved both during day and night. Vertical smoothing is applied through a moving mean (window length of 210 m) improving the signal-to-noise ratio. The bottom and top heights of the aerosol layers were obtained by using the gradient method (Flamant et al., 1997; Papayannis et al., 1998), which enables the location of regions in the atmosphere characterised by rapid changes in the backscattered radiation that may be associated with variations in aerosols (density or size) and humidity (Flamant et al., 1997; Granados-Muñoz et al., 2015). The backscatter- and extinction-related Ångström exponents for the different wavelength sets (355–532 nm, 355–1064 nm and 532–1064 nm) and the particle lidar ratio profiles were derived from the measured backscatter and extinction coefficient profiles. The layer aerosol optical depth at 532 nm (AOD_L^{532}) was calculated from the extinction coefficient measurements integrated between the bottom and the top height of the aerosol layer. During daytime, the AOD_L^{532} was obtained by integrating the extinction coefficients calculated by using the daily mean lidar ratio and the backscatter coefficient measurements (Preißler et al., 2011).

2.3.2. Polarized Micro-Pulse Lidar

The polarized Micro-Pulse Lidar (P-MPL) system is an elastic lidar that measures the atmospheric backscatter signal and volume depolarization at 532 nm with 1-min integration time and 75-m vertical resolution, as those required in MPLNET (Welton et al., 2001), operating continuously (24/7) for vertically-resolved monitoring of aerosols and clouds. Main technical details about the MPL systems installed at El-Arenosillo/Huelva (ARN) and Barcelona (BCN) can be found, for instance, in López-Cayuela et al. (2021) and Córdoba-Jabonero et al. (2019), respectively. In this work, the raw MPL data were processed manually offline using validated procedures (Campbell et al., 2002; Córdoba-Jabonero et al., 2018, 2019, 2021; Flynn et al., 2007; Sicard et al., 2020) in order to obtain the range-corrected signal (RCS), which is the particular lidar variable in combination with the sun-photometer data to be used as input in GRASP. MPLNET cloud products were obtained for cloud-screening of the MPL signals.

2.3.3. Ceilometers

The CHM15k-Nimbus ceilometers (Lufft manufacturer) work as one-wavelength lidar providing measurements of the atmospheric backscatter signal at 1064 nm. The measurements are available at different altitudes up to 15 km above ground level, with vertical resolutions of 15 m (Cazorla et al., 2017). Ceilometers at Granada (UGR), Guadiana-UGR (GDN) and Madrid (MAD) provide measurements with a temporal resolution of 15 s, while Badajoz (BDJ) operates at a temporal resolution of 1 min. According to the manufacturer, the overlap of the telescope and the laser beam is 90% complete between 555 and 885 m above ground level. A complete overlap is found at 1500 m above the instrument (Heese et al., 2010). Technical details and more information about the CHM15k-Nimbus ceilometers and its products can be found at Lufft (2021). The ceilometer data at these stations are managed by ICENET (Cazorla et al., 2017), and the used data were obtained directly from this network.

2.3.4. Sun-photometers

The CIMEL CE-318 sun-photometers can measure direct Sun irradiances and sky radiances at different wavelengths in ultraviolet, visible and near-infrared spectral regions. Direct irradiance measurements are used to calculate the spectral AOD and the Ångström exponents, while the combination of direct irradiances with sky radiances are used as inputs in inversion algorithms (e.g., Dubovik et al., 2006; Dubovik and King, 2000) to retrieve aerosol size distribution and aerosol optical and microphysical properties. In this work, the measurements used were sky radiances and AOD only at 440, 675, 870 and 1020 nm because these wavelengths are available in most AERONET sun-photometers. These data correspond to the level 1.5 data (automatically filtered to eliminate cloud effects) processed with the AERONET algorithm version 3 (Giles et al., 2019). For the MPL and ceilometer inversions combined with sun-photometer, the values of AOD and sky radiances used were obtained from CAELIS (Fuertes et al., 2018; González et al., 2020) instead of AERONET. CAELIS is a software tool developed by the Group of Atmospheric Optics at the University of Valladolid (GOA-UVa), to manage data from the Iberian Network for Photometric Measurement of Aerosols and to investigate aerosol properties over Europe. Cloud-screened AOD and sky radiances from both AERONET and CAELIS databases are similar as demonstrated in González et al. (2020).

2.4. GRASP retrievals

The Generalized Retrieval of Aerosol and Surface Properties code (GRASP; Dubovik et al., 2014, 2021) is an open-source and versatile algorithm that permits the combination of several remote sensing measurements. In this work, GRASP was applied to the combination of sun-photometer and one-wavelength lidar/ceilometer data to retrieve column integrated and vertically resolved aerosol properties (López-Cayuela et al., 2021, 2022; Román et al., 2018) for the different sites referred in Table 1. GRASP allows for the use of multi-wavelength elastic lidar combined with AERONET sun-photometer measurements that permits more advanced retrieval by separating between fine and coarse mode properties and their vertical distribution (e.g., Benavent-Oltra et al., 2021; Lopatin et al., 2013, 2021). These GRASP retrievals are only available during daytime when AERONET measurements are available.

In this work, the two previous GRASP approaches were applied to different sites, depending on their lidar system characteristics (Table 1). This permits taking advantage of the maximum synergy between instruments. Range corrected signals (RCS) measured by the multi-wavelength lidar (355, 532 and 1064 nm), P-MPL (532 nm) and ceilometer (1064 nm) were cloud-screened and averaged for 30 min around the co-located AERONET sun-photometer sky radiance measurements.

The MPL and ceilometer retrievals (vertical single-wavelength) were done following the method proposed by Román et al. (2018) but using the sun-photometer data from CAELIS instead of AERONET. In fact, the retrievals based on ceilometer data were automatically calculated by CAECENET (Román et al., 2021), which is an automatic system that inverts data from ICENET (ceilometer) and CAELIS (sun-photometer) with GRASP (method of Román et al., 2018) in near-real-time (Bazo et al., 2023). The use of products already processed from CAECENET is the main reason for the use of CAELIS data in the single-wavelength lidar inversions instead of AERONET ones.

The Cerro-Poyos sun-photometer dataset was combined with the ceilometer installed at the Granada site which is about 12 km away (horizontally). The GRASP output variables (vertically-resolved and column integrated) used in this work are the total volume concentration, the total backscatter and extinction coefficients, aerosol optical depth, Ångström exponent, volume size distributions, and single scattering albedo. After selecting the GRASP profiles, the bottom and top heights of the VA layer and the layer AOD were obtained following the methodology described in section 2.3.1.

3. Results

3.1. Volcanic ash plumes from satellite retrievals

Fig. 1 shows the temporal series of the area affected by the volcanic plume and the volcanic aerosol cloud maximum altitudes for the periods of eruptive activity, obtained from MODIS retrievals (subsection 2.1). The volcanic ash plume was horizontally distributed over a reduced area mostly near the volcanic cone with a mean value of 120 ± 202 km^2. The irregularity in the volcanic activity and the synoptic situation led to some variability in the areas affected by the volcanic ash aerosols, ranging from 11 km^2 to 974 km^2 on 18 and 31 October 2021, respectively. On the other hand, an intense volcanic phase occurred from 30 October to 2 November, with plumes even larger than 300 km^2 (Fig. 2).

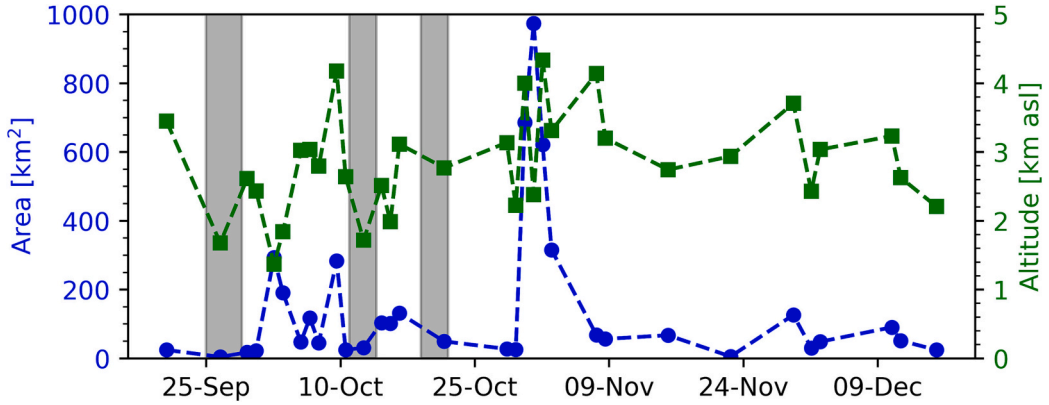

Fig. 1. Temporal series of the ash cloud maximum altitude (green squares) and the ash cloud horizontal extension (blue circles) for the whole Tajogaite eruptive activity period (19 September to 13 December 2021). The grey-shaded rectangles represent events I, II and III presented in this work. (For interpretation of the references to colour in this figure legend, the reader is referred to the web version of this article.)

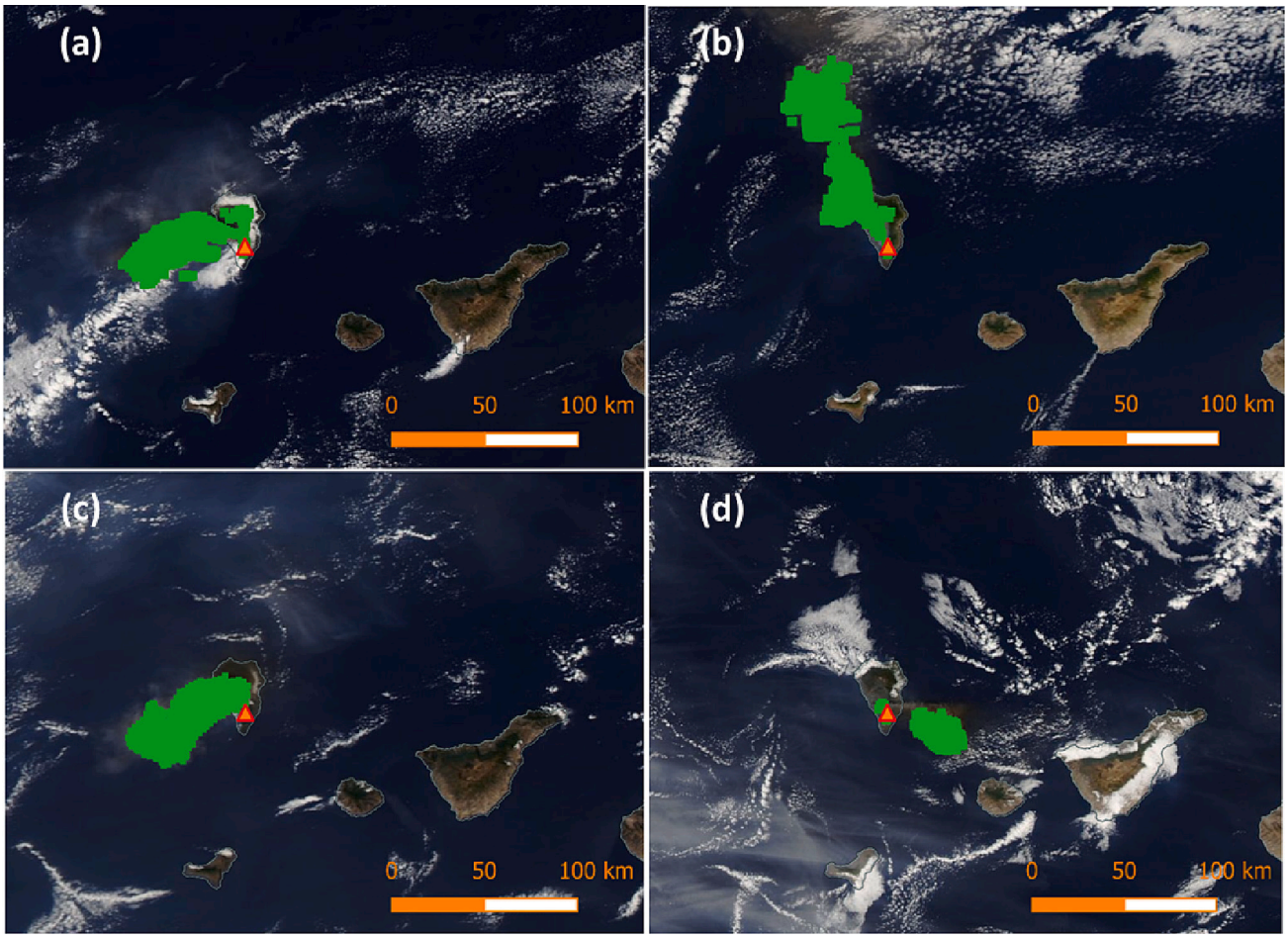

Fig. 2. Volcanic ash clouds (green area) the MODIS/Aqua reflectance scenes over the Canary Islands during the intense volcanic phase occurred from 30 October to 2 November: (a) 30 October, (b) 31 October, (c) 1 November and (d) 2 November 2021. The orange triangle represents the Tajogaite volcano location. (For interpretation of the references to colour in this figure legend, the reader is referred to the web version of this article.)

During the afternoon of 29 October, a series of intense and successive explosions, accompanied by some earthquakes, occurred for several hours generating the injection of large amounts of volcanic ash and SO_2 in the atmosphere, which were maintained until 2 November, as reported by the Global Volcanism Program (2021). Fig. 2 shows MODIS/Aqua reflectance images, which clearly reveal the intense volcanic eruption (shaded green areas in the figures).

The volcanic ash plume top-heights were in the low and middle troposphere during the whole volcanic eruptive activity (mean values of 2800 ± 700 m asl), ranging from a minimum of 1365 m asl on 2 October to a maximum of 4333 m asl on 1 November (during the most intense volcanic phase). The volcanic ash plume top-heights were more variable, between 1500 and 3000 m asl, from the beginning of the eruption until 15 October, while the top-height remained above 2000 m asl

during the rest of the volcanic eruption. Similarly, to the ash plume area, the volcanic ash plume top-height showed the maximum values in the period from 29 October to 2 November. Due to the intensification of volcanic activity during those days, the local authorities alerted the population regarding air quality degradation and recommended staying indoors and wearing filter masks (Global Volcanism Program, 2021). These values agree with those presented by Sicard et al. (2022) and Córdoba-Jabonero et al. (2023) who used an elastic lidar system in

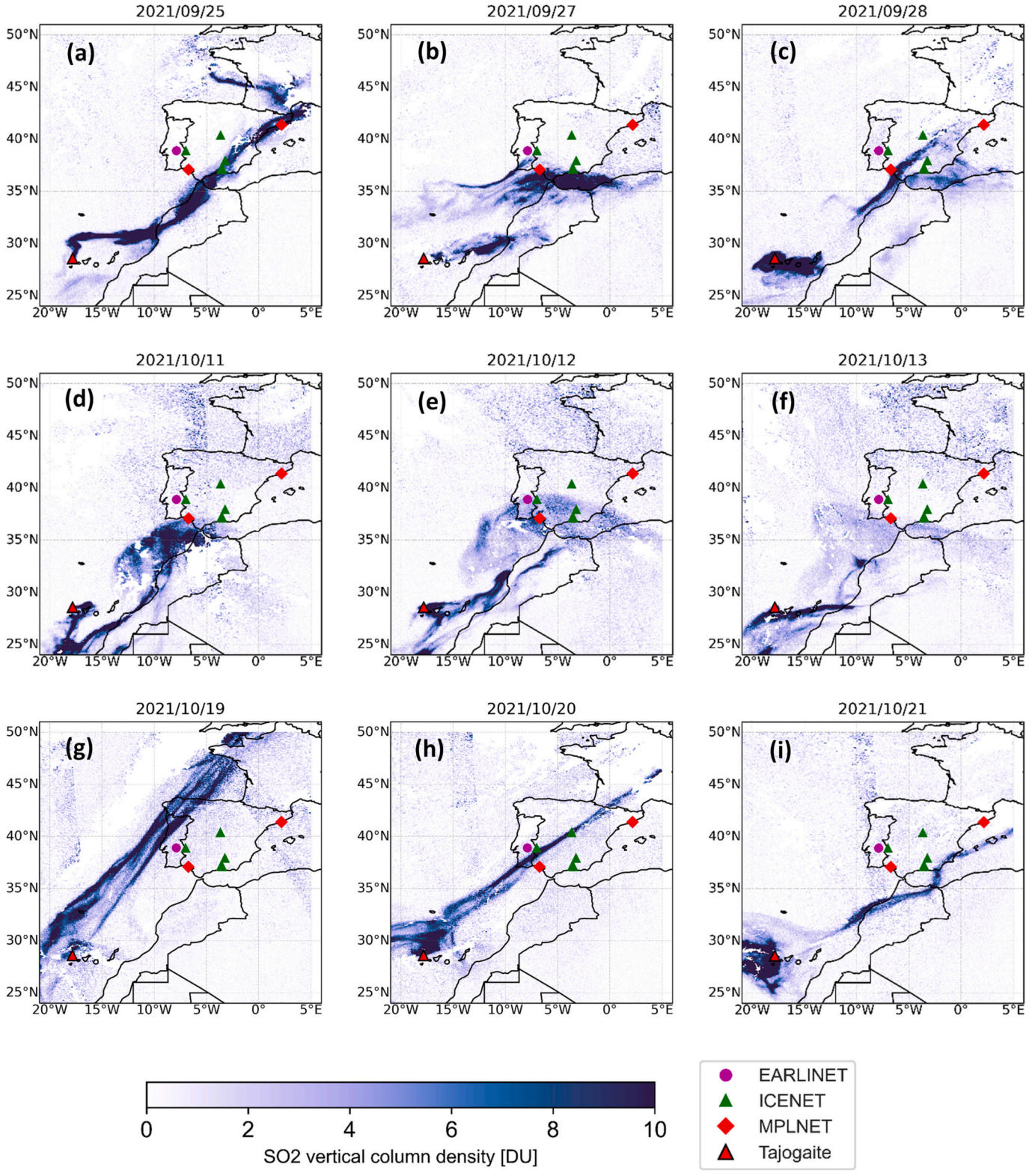

Fig. 3. TROPOMI SO_2 tropospheric column concentration observed from 25 to 28 September (event I), 11–13 October (event II) and 19–21 October (event III). The symbols for EARLINET, ICENET and MPLNET represent the sites with the used lidar/ceilometer instrumentation that integrate the different networks. The geographic location of the Tajogaite volcano is represented by a red triangle. (For interpretation of the references to colour in this figure legend, the reader is referred to the web version of this article.)

Tazacorte (La Palma Island), specifically for the Tajogaite monitoring (10 km in horizontal distance from the volcanic emission source). In particular, Sicard et al. (2022) reported a mean volcanic ash plume top-height of 1400 ± 500 m asl from 16 October to 31 December (second period aforementioned). On 15 November two volcanic ash plumes were detected, one at 2000 m and a thinner one at 2741 m asl (the maximum altitude reported by those authors).

During the last two decades, other European volcanoes have also injected volcanic aerosols into the atmosphere at different altitudes depending on the volcanic structure and the VEI. Arason et al. (2011) reported volcanic ash plume top-heights mostly above 3000 m asl with some scattered values up to 10,000 m asl during the eruption of the Eyjafjallajökull in 2010. The lower volcanic ash plume top-height during the Tajogaite eruption, with a VEI of 3 and emission height of 1124 m asl, was expected to be comparable to the Eyjafjallajökull episode, with a VEI of 4 (more explosive) and an emission height of 1650 m asl. Corradini et al. (2008) analysed the Mt. Etna eruption, that occurred on 24 November 2006, using the same methodology presented in section 2.1, revealing volcanic ash plume top-heights around 5000 m asl, because, despite having a VEI of 2, the emission height was considerable larger (3365 m asl) than the Tajogaite (1121 m).

3.2. Transport of volcanic plumes towards the Iberian Peninsula

Fig. 3 shows TROPOMI Sentinel-5P observations over the IP allowing for the identification of Tajogaite volcanic plume transports. For the entire eruption period (19 September - 13 December 2021) three different events were detected over the IP: The first event occurred from 25 to 28 September (designated as event I), the second from 11 to 13 October (event II) and third from 19 to 21 October (event III). Fig. 3 shows SO_2 vertical column density for the three different events while Fig. S1, in the supplementary material, shows wind speeds and directions at 700 hPa for some representative days of these events. Specific details of each event are:

Event I: on 25 September, an elongated and narrow SO_2 plume with values around 10 DU was identified (Fig. 3a). This plume extended from the volcano to the south of France crossing the south and southeast of IP and passing over some of the considered observation sites. The plume moved to the south of IP on 26 September (figure not shown). Finally, on 27–28 September, the plume split up, becoming more spread and reaching again some of the observation sites (Fig. 3b and c). On 24 September the development of a low-pressure system centred near the Portuguese coast (40°N, 10°W) favoured the SW winds and, therefore, the transport of volcanic plume from the Canary Islands (Fig. S1a). The low-pressure system moved Northward and dissipated on 25 September (Fig. S1b) favouring the intrusion of a westerly flow over the IP and the displacement of the elongated band eastward from the IP sites on 26 September. In the next few days, 27–28 September, the atmospheric flow (figures not shown) induced the volcanic plume concentration in southern IP until it dissipated.

Event II: the identified volcanic plume followed a similar path as in the event I, extending volcanic emissions from the volcano to the south of IP (Figs. 3d and f). In this event, the plume showed a more dispersed shape and covered a larger area in IP, mainly on 12 October, when all the observation sites located in the south of IP were covered by the plume with SO_2 values between 4 and 8 DU. Later, the volcanic plume started to dissipate. The synoptic situation observed shows a low-pressure system at 700 hPa centred northeast of the Madeira Archipelago on 11 October (Fig. S1c) producing the westerly winds over the Canary Islands with velocities of about 8 m s^{-1}. Over the Sahara Desert, the presence of a high-pressure system centred around 24°N and 1°E/5°W was identified (Fig. S1c and S1d). These two circulation systems induced the south-westerly flow along the African coast extending to the south of the IP transporting the volcanic plume.

Event III: on 19 October, the TROPOMI SO_2 observations showed an elongated plume with values around 10 DU extending over the Atlantic Ocean from Canary Island to the north of France crossing the north of the IP (Fig. 3g). The plume became narrow and less dense as it moved in the NW-SE direction crossing the IP on 20 October (Fig. 3h). Finally, on 21 October the plume crossed all the IP starting to dissipate (Fig. 3i). On 19 October, there were two low-pressure systems at middle levels, centred at 34°N/7°W and 24°N/21°W, respectively (figure not shown). Such synoptic conditions favoured the south-easterly flow on the Canary Islands, which extended up to 32°N and changed direction towards the IP (Fig. S1e). Changes in flow directions with time to the southwest with a wind speed of up to 10 ms^{-1} explain the changes in the transported volcanic plumes. On 21 October (Fig. S1f), north-westerly winds prevailed over the IP when the plume crossed it.

3.3. Aerosol properties from Klett-Fernald and Raman retrieval methods

Fig. 4a and b show the temporal evolution of the range corrected signal (RCS) at 1064 nm observed by Raman lidar over Évora and associated with events II and III, respectively. The event I was not detected over Évora. For event II, Fig. 4a shows the evolution from 11 October at 18:00 UTC to 13 October at 12:00 UTC. The most relevant feature is the presence of an aerosol layer extending between 2.5 and 5 km asl, decoupled from the atmospheric boundary layer (ABL), and observed from 22:00 UTC on 11 October to 06:30 UTC on 13 October. This upper-level layer is associated with the volcanic plume that crossed the IP during event II. The RCS also shows the presence of some high-altitude clouds above the volcanic plume early in the morning and around noon on 12 October. For event III, Fig. 4b shows the RCS evolution from 19 October at 18:00 UTC to 20 October at 18:00 UTC, revealing the presence of an aerosol layer located between 2.5 and 3.5 km asl from 00:00 UTC to 12:00 UTC on 20 October that is again associated with the volcanic plume that crossed the IP during event III. This upper-level layer is thinner and shorter than the volcanic plume observed during event II. Below the volcanic plume, the ABL can be observed and after 12:00 UTC the plume seems to mix with the ABL until it vanishes. During event III, high clouds located between 7.5 km and 12.5 km asl were observed almost during the whole event. In summary, for both events, the RCS observations agree with the TROPOMI SO_2 observations (Fig. 3) and with the 144 h (6-day) HYSPLIT backward-trajectories ending at 22:00 UTC on 11 October and at 00:00 UTC on 20 October (Fig. S2 in the supplementary material) that confirm the provenance of the volcanic aerosols at heights detected by the lidar.

Fig. 5 illustrates the temporal evolution of the volcanic aerosol layer observed with Raman lidar measurements (2.5–5.0 km asl) from 11 to 13 October in terms of backscatter coefficient at 532 nm (β_{532}), linear particle depolarization ratio (δ_p) and backscatter-related Angström exponent for the wavelength pair 532–1064 nm (β-$AE_{532/1064}$). The β_{532} values ranged approximately between 1 and 2.5 Mm^{-1} sr^{-1} in the central region of the VA layer with maximum values taking place on 12 October. The δ_p presents low values, approximately between 0.05 and 0.10, during the whole event. These seem to decrease from 11 to 12 October, varying between mean values of 0.10 at the beginning of the event to a minimum mean value of 0.06 at 16:30 UTC on 12 October. Later, during the evening on 12 October, δ_p starts to increase, reaching a maximum mean value of 0.11 at 00:00 UTC on 13 October. The β-$AE_{532/1064}$ presents variability during the event, with mean values ranging from 1.01 on 11 October at 23:30 UTC to 1.91 on 12 October at 07:30 UTC. These results, low δ_p and high β-$AE_{532/1064}$ values, suggest the predominance of small spherical particles at the observation site during the whole event, which can be associated with sulphate particles from the transported volcanic plume. Besides, as shown in section 3.1, the volcanic ash plume area was horizontally distributed near the volcano cone (120 ± 202 km^2) during the whole eruptive activity. The described evolution of δ_p and β-$AE_{532/1064}$ also indicates a slight variation in the shape and size of the particles present in the atmosphere.

Fig. 6 shows the frequency distribution of the properties of the VA layer observed during event II (2.5–5.0 km asl). The β_{532} (Fig. 6a)

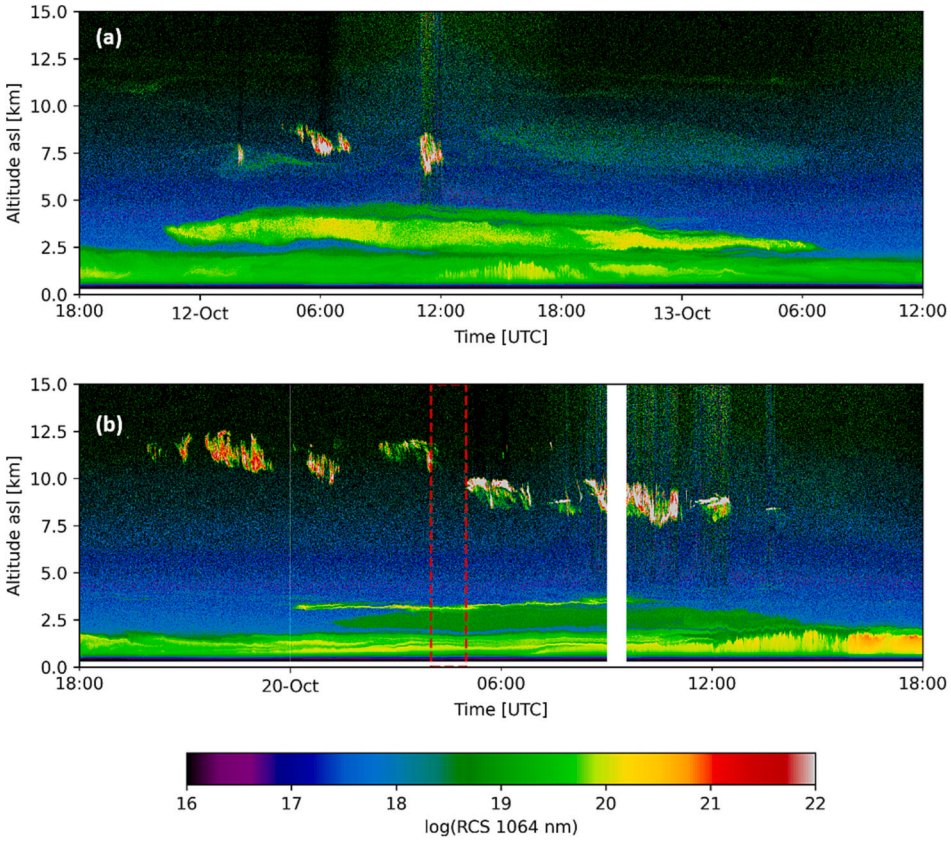

Fig. 4. Time series of range corrected signal at 1064 nm (in arbitrary units) observed over Évora with a Raman lidar: (a) from 18:00 UTC on 11 October to 12:00 UTC on 13 October 2021 and (b) from 18:00 UTC on 19 October to 18:00 UTC on 20 October 2021. In (b), the white area corresponds to a gap in the data measurements and the red dashed area indicates the period of the mean profiles illustrated in Fig. 8. (For interpretation of the references to colour in this figure legend, the reader is referred to the web version of this article.)

presents a bimodal distribution with one peak around 0.5 Mm^{-1} sr^{-1} and a second one around 1.5 Mm^{-1} sr^{-1}. The distribution of the particle depolarization ratio (Fig. 6b) shows most of the values occurring between 0.06 and 0.10 (76% of the data). The lidar ratio at 532 nm (LR_{532}) also presents a bimodal distribution (Fig. 6c) with the first major peak around 50 sr with 59% of the data occurring in the range 40–60 sr, while the second and minor mode peak around 80 sr with 7% of data occurring in the range 80 ± 6 sr. The distribution of β-$AE_{532/1064}$ (Fig. 6d) shows most of the values occurring between 1.05 and 1.76 (90% of the data). The results agree with values observed for tropospheric particles from the Eyjafjallajökull volcanic plumes detected over the IP in 2010 (Navas-Guzmán et al., 2013; Sicard et al., 2012). For example, Navas-Guzmán et al. (2013) reported mean values of linear particle depolarization ratios between 0.04 and 0.07, β-$AE_{532/1064}$ between 0.7 and 1.7 and similar lidar ratios for both wavelengths 355 and 532 nm of around 50 sr in the centre of the layers observed over Granada station. On the other hand, Sicard et al. (2012) reported mean values of LR_{532} (β-$AE_{532/1064}$) for the optically thickest layers observed over Évora of 32 ± 4 sr (1.05 ± 0.43). These low values of LR_{532} were attributed to the plume transport at altitudes well above 3 km from Iceland to the IP over the Atlantic Ocean (approx. 3000 km distance, while Tajogaite is approx. 1500 km) and air mass dehydration along the path, which leads to a decrease of the lidar ratio. Still, the LR_{532} values reported by Sicard et al. (2012) for Madrid and Granada of 52 ± 27 sr and 48 ± 16 sr, respectively, agree well with the observations reported in this work.

Fig. 7 shows the temporal evolution of the VA layer aerosol optical depth at 532 nm (AOD_L^{532}) (obtained integrating into the range 2.5–5.0 km asl). The AOD_L^{532} ranged from 0.02 to 0.18 during the event, reaching its maximum value on 12 October. Compared with the total column AOD at 532 nm (AOD_C^{532}) obtained from the co-located AERONET station, on 12 October the AOD_L^{532} contribution varied from 49% to 82% of the total column AOD_C. In terms of AOD_L^{532} and AOD_C^{532} mean values (0.12 ± 0.02 and 0.19 ± 0.01, respectively) the contribution was 63%. The maximum value of AOD_L^{532} (0.18) is rather large compared with the value of 0.07 reported by Sicard et al. (2012) for an optically thick VA layer observed in Évora in 2010. To note, the maximum value of 0.18 reported in this study corresponds to a layer thickness of 2.13 km, which is about twice the value for the layer thickness reported by Sicard et al. (2012). On the other hand, for volcanic aerosols in the stratosphere over the IP, (Sawamura et al., 2012) reported AOD_L^{532} of 0.02 at Granada station for plumes transported from the Nabro volcano in Ethiopia and contributions to the co-located AERONET of about 5% at 532 nm.

During event III, on 20 October, the cloud presence prevents lidar retrievals (see Fig. 4b), leading to only a few profiles retrieved during the night and in the early morning. Fig. 8 shows 1-h mean vertical profiles of the volcanic aerosol properties on 20 October from 04:00 UTC to 05:00 UTC (red box in Fig. 4b) as representative and trustworthy observed lidar profiles of this event. The volcanic aerosol layer extends from about 2.8 km to 3.4 km asl as highlighted by the shadowed area. The profiles show β_{532}, δ_p and β-$AE_{532/1064}$ that fit in the same variation ranges as the event II. In addition, the extinction coefficient at 532 nm (α_{532}) and the LR_{532} vary in the ranges from 29 to 41 Mm^{-1} and 36–50 sr, respectively. The variation ranges lower limit of the measured LR_{532} is slightly lower. Despite that, the LR_{532} is in the range of 30–45 sr reported by Mattis et al. (2010) for volcanic plumes observed in the stratosphere over central Europe. Also, the volcanic plume followed a different path from the event II, which can imply interaction with different aerosol sources and, consequently, different aerosol mixtures.

Table 2 summarises the main VA properties observed from Raman lidar for events II and III. The mean values clearly agree with the temporal evolution of the layer properties observed from 11 to 13 October described previously. Event II was the most intense reaching its maximum intensity on 12 October with AOD_L^{532} mean values of 0.12 ± 0.02 for a mean layer thickness (Δz) of 1.83 ± 0.27 km, while in event III, on 20 October, the mean value was 0.02 ± 0.01 for the available profiles with Δz of 0.49 ± 0.12 km. The δ_p was similar in both events

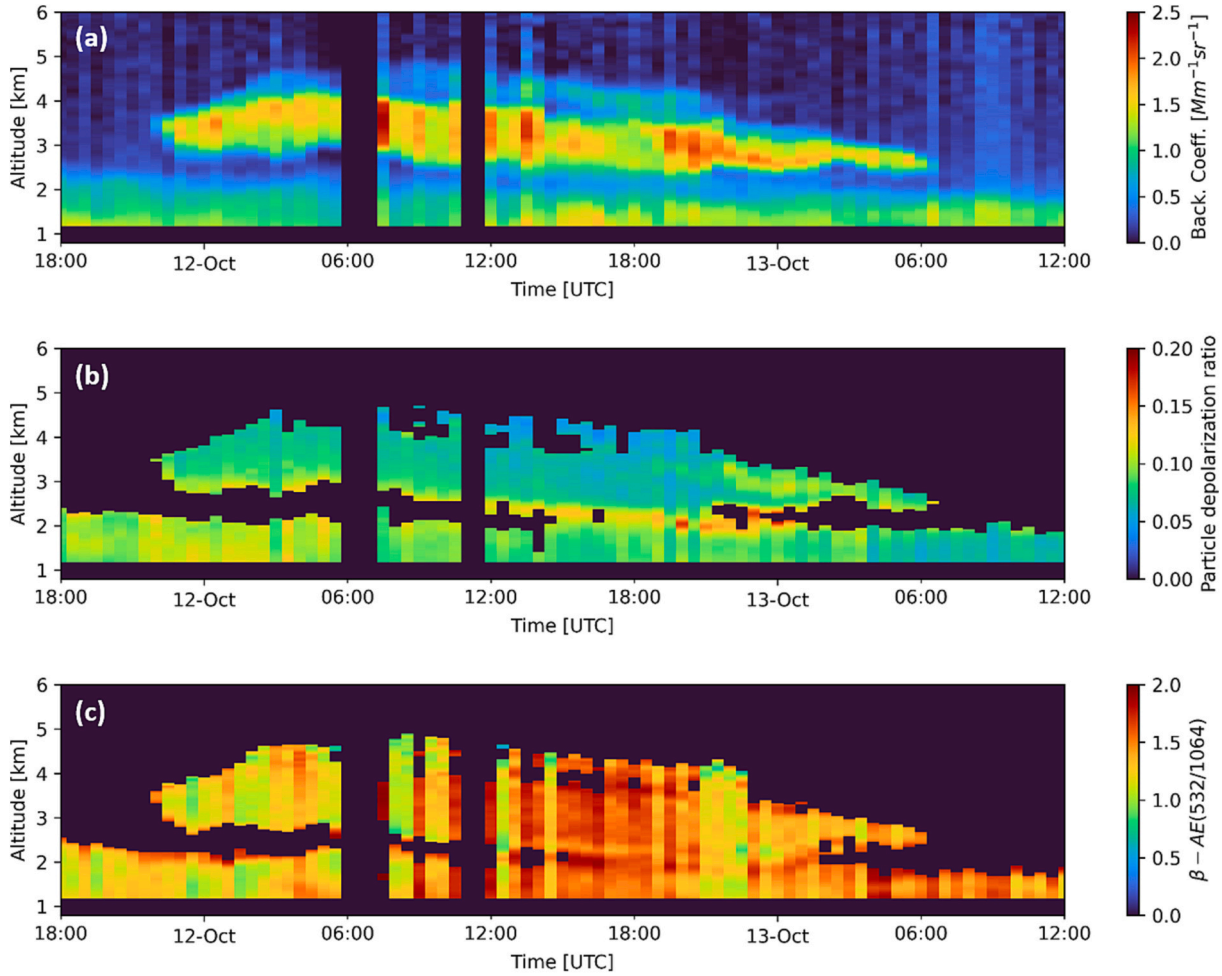

Fig. 5. Time series of particle properties observed by Raman lidar over Évora: (a) particle backscatter coefficient at 532 nm, (b) linear particle depolarization ratio and (c) backscatter-related Ångström exponent for the wavelength pair 532–1064 nm. The gaps in the layer (from 06:00 to 07:30 UTC and from 11:00 to 12:00 UTC on day 12) correspond to the periods where lidar retrievals were not possible due to the cloud presence.

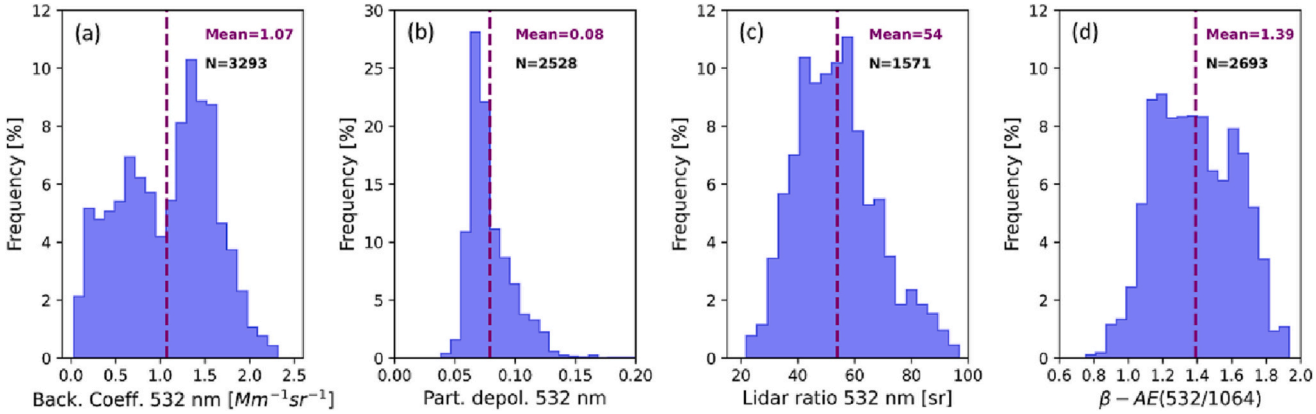

Fig. 6. Distributions of the VA layer properties (2.5–5.0 km asl) observed by Raman lidar from 11 to 13 October: (a) backscatter coefficient at 532 nm, (b) particle depolarization ratio at 532 nm, (c) lidar ratio at 532 nm and (d) backscatter related Ångström exponent for the wavelength pair 532–1064 nm.

with mean values from 0.08 ± 0.02 to 0.09 ± 0.02 and of 0.09 ± 0.02 for event II and III, respectively, suggesting the predominance of spherical particles. Also, the mean β-$AE_{532/1064}$ suggested the predominance of small particles in both events, taking the mean values from 1.17 ± 0.20 to 1.40 ± 0.24 (event II) and of 1.25 ± 0.20 (event III). The mean lidar ratios were slightly smaller in event III (46 ± 10 sr) than in event II (54 ± 14 sr), which can be due to the different transport paths followed by the plumes and, consequently, different interactions with other anthropogenic emission sources (Sicard et al., 2012). Another explanation could be the differences in relative humidity and temperature and, consequently, hygroscopic growth (Perez-Ramirez et al., 2021).

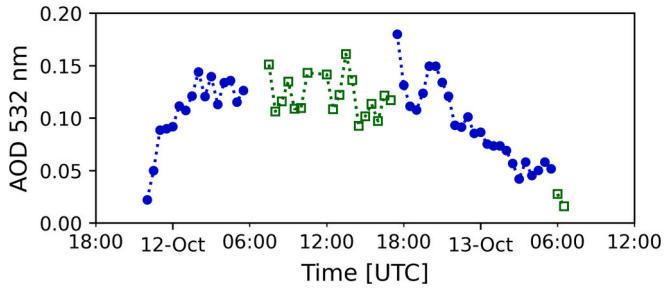

Fig. 7. Temporal series of the layer aerosol optical depth at 532 nm obtained by integrating the extinction coefficients from Raman lidar measurements (night time; blue circles) and the elastic backscatter coefficient and mean lidar ratio (day time; open green squares). (For interpretation of the references to colour in this figure legend, the reader is referred to the web version of this article.)

3.4. Aerosol properties from GRASP retrievals

3.4.1. Aerosol properties in the atmospheric column

Aerosol properties in the atmospheric column are discussed here to give an overview of the aerosols present in the atmosphere over the stations during the events. Fig. 9 shows the distributions of the aerosol optical depth at 400 nm (AOD_C^{440}) and the corresponding Ångström Exponent for the wavelength pair 440–870 nm ($AE_{440/870}$) at the stations where the volcanic plumes were identified during events I (Fig. 9a and c) and II (Fig. 9 b and d). During event III, only four occurrences of plumes were identified in a total of three stations, which does not provide useful information in terms of boxplots of the AOD_C^{440} and $AE_{440/870}$ distributions. The results show that Guadiana, Granada and Cerro-Poyos present high variability of AOD_C^{440} during both events (I and II). This variability in the data can be explained by the duration and number of occurrences of plumes' detection, since different days/times may present different aerosol content in the atmosphere, and, additionally, the AOD_C^{440} is influenced by the ABL. On the other hand, Badajoz presents low variability in AOD_C^{440} and Évora presents almost no variability. In these two specific cases, the identification of the volcanic plumes from GRASP retrievals was only possible on 12 October. The AOD_C^{440} mean values range between 0.12 and 0.37 at El-Arenosillo/Huelva and Guadiana, respectively, in event I and between 0.25 and 0.39 at Cerro-Poyos and Guadiana, respectively, in event II. More detail about AOD_C^{440} mean values per day and per station can be found in the supplementary material (Table S1 in supplementary material). The distributions of $AE_{440/870}$ show all values above 1 at all stations, in both events, indicating the presence of small particles in the atmospheric column. The mean values ranged between 1.15 (in Barcelona) and 1.59 (in Cerro-Poyos), in event I and between 1.19 (in Granada) and 1.44 (in Évora) during event II. As for event III, the $AE_{440/870}$ varies between 1.03 and 1.33, corresponding to AOD_C^{440} of 0.11 and 0.12 for the available profiles.

Fig. 10 shows volume size distributions corresponding to several cases of volcanic plumes identified during events I and II. The size distributions present a bimodal shape in both events with the fine mode dominating over the coarse mode at several stations during event I, mainly on 25 September. In event II, El-Arenosillo/Huelva station can give some insights about the particle evolution with an increase in the fine mode from 11 to 12 October, when it reached maximum values, and then decreases again. During event III, the size distributions (Fig. S3 in

Table 2
Mean values and the standard deviation of the volcanic aerosol layer properties for all the available profiles measured by Raman lidar during Events II and III. The mean values of AOD_{532}^L are for the data represented in Fig. 7. In the table, the aerosol property marked with an * represents night time averages, while all others are for daily mean values.

Aerosol property	Event II			Event III
	11th Oct	12th Oct	13th Oct	20th Oct
β_{532} (Mm^{-1} sr^{-1})	0.7 ± 0.5	1.1 ± 0.5	0.9 ± 0.5	0.6 ± 0.3
α_{532} (Mm^{-1}) *	47 ± 22	67 ± 24	57 ± 17	42 ± 16
LR_{532} (sr) *	53 ± 12	54 ± 15	52 ± 14	46 ± 10
δ_p	0.09 ± 0.01	0.08 ± 0.02	0.09 ± 0.02	0.09 ± 0.02
β-$AE_{532/1064}$	1.17 ± 0.20	1.40 ± 0.24	1.40 ± 0.13	1.25 ± 0.20
AOD_{532}^L	0.063 ± 0.033	0.121 ± 0.021	0.056 ± 0.019	0.021 ± 0.007
Δz (km)	1.3 ± 0.3	1.8 ± 0.3	1.1 ± 0.2	0.5 ± 0.1

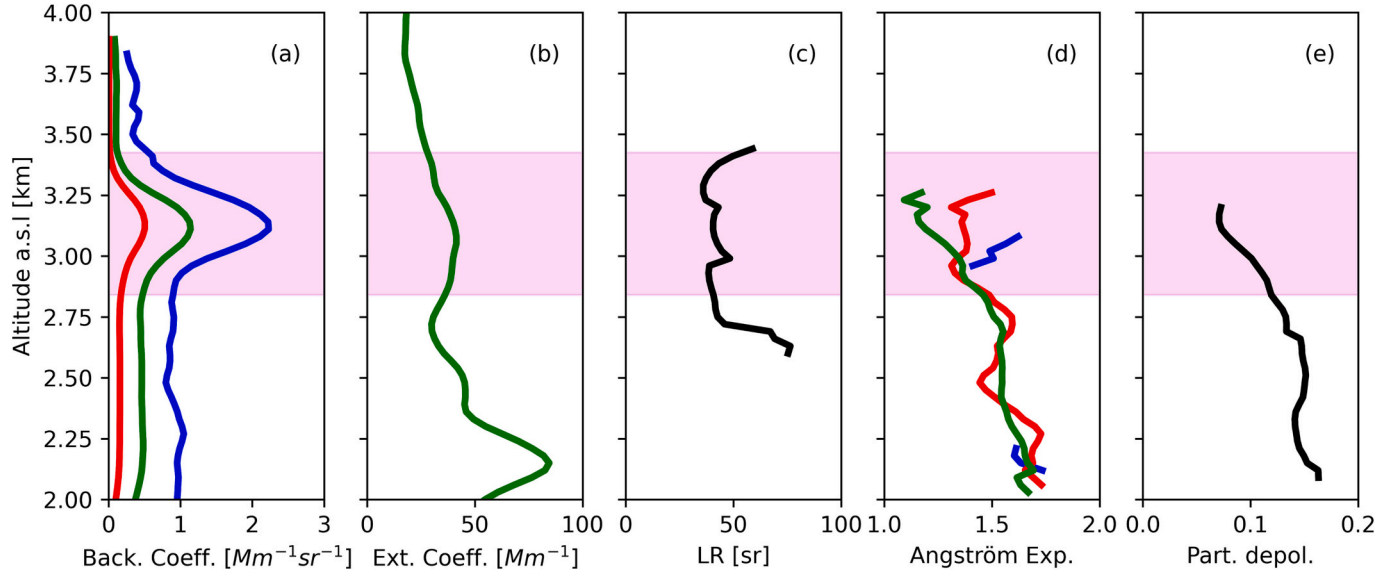

Fig. 8. The 1-h mean values of the VA optical properties derived from the Raman lidar measurements on 20 October from 04:00 to 05:00 UTC: (a) Particle backscatter coefficients (355 nm in blue, 532 nm in green and 1064 nm in red), (b) extinction coefficient at 532 nm, (c) lidar ratio at 532 nm, (d) backscatter related Ångström exponents (355–532 nm in blue, 532–1064 nm in green and 355–1064 nm in red) and (e) particle depolarization ratio at 532 nm. The volcanic aerosol layer between 2.8 km and 3.4 km asl is highlighted by the shadow area. (For interpretation of the references to colour in this figure legend, the reader is referred to the web version of this article.)

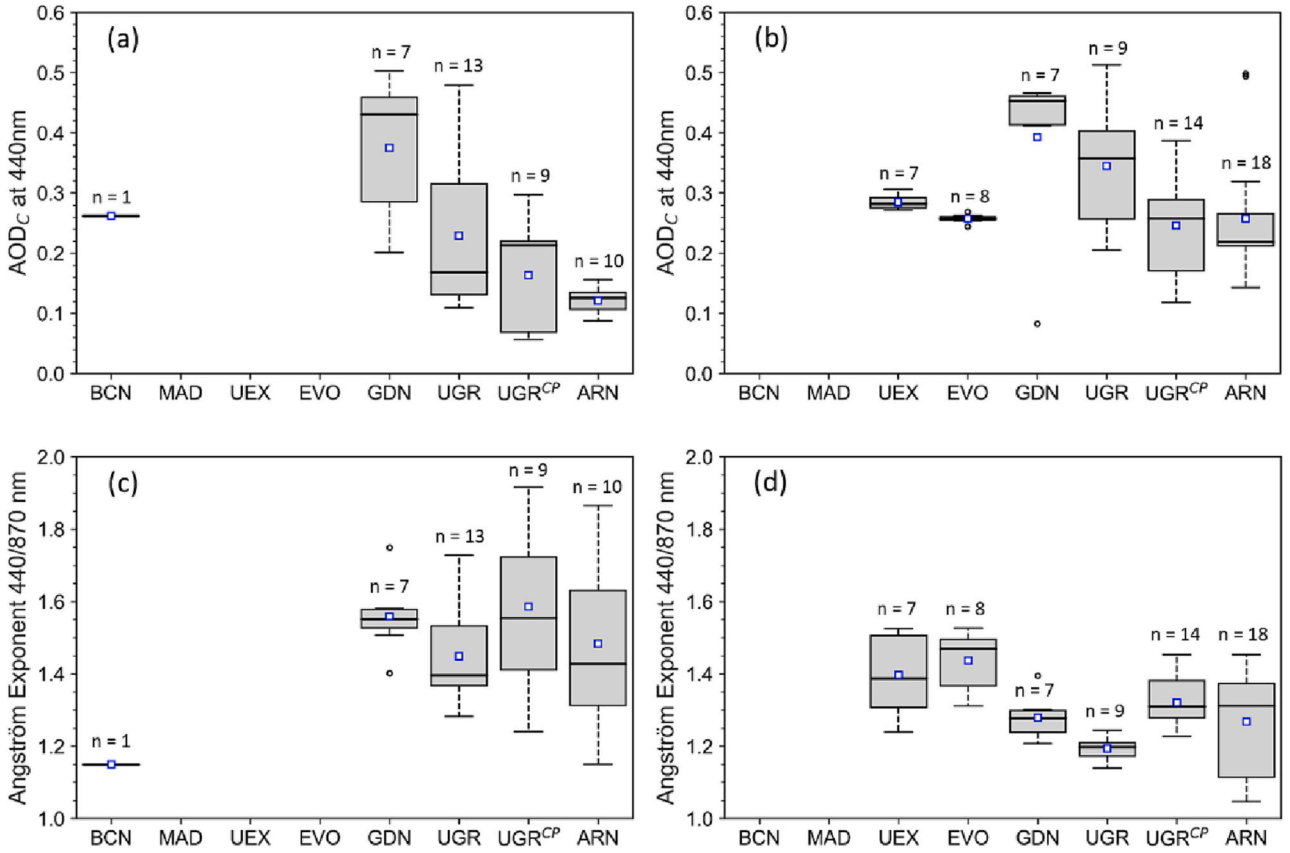

Fig. 9. Aerosol optical depth and Ångström exponent in the atmospheric column at the different sites for the periods when the volcanic plumes were detected in events I, (a) and (c), and II, (b) and (d). The blue square represents the mean value, the black line represents the median and the whiskers show the maximum and minimum values. (For interpretation of the references to colour in this figure legend, the reader is referred to the web version of this article.)

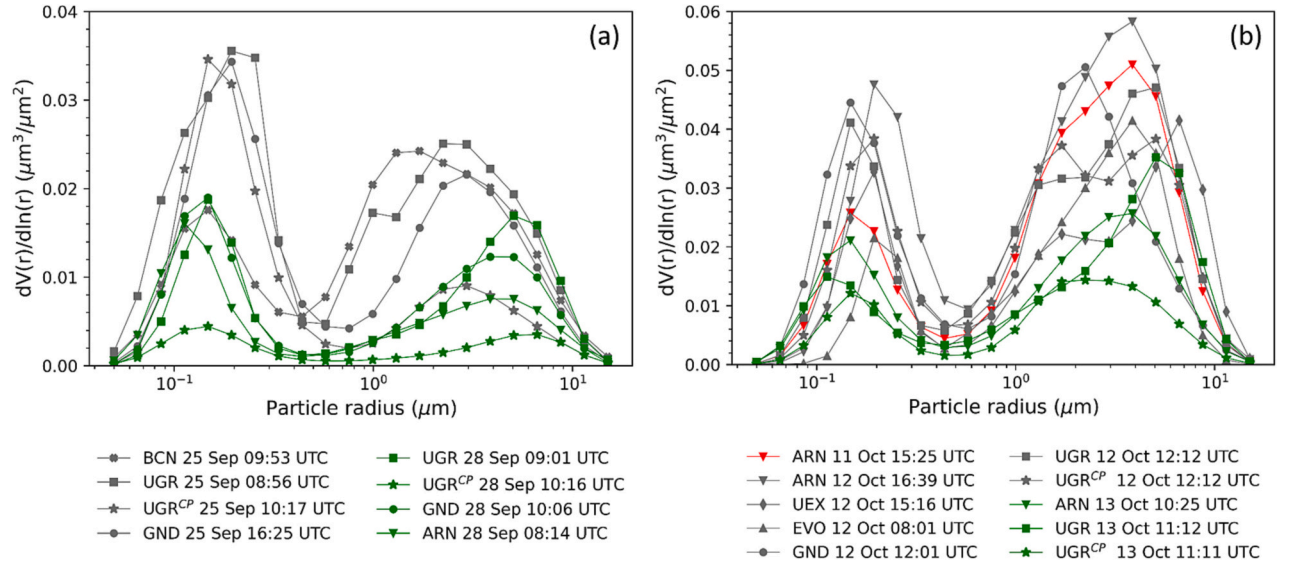

Fig. 10. Aerosol volume size distributions from sun-photometer measurements, for 22 logarithmically equidistant bins in the radius range from 0.05 to 15 μm, taken at the different stations for several time in: (a) event I and (b) event II.

the supplementary material) corresponding to the identified layers, also present a bimodal shape but with a less pronounced fine mode than in events I and II. This may be connected to the smaller number of observations available.

3.4.2. *Volcanic plume profiling*

Figs. 11-13 show the profiles of the particle backscatter coefficients at 440 nm (β_{440}) and the total volume concentrations (VC) obtained from the one-wavelength lidar (P-MPL lidar and ceilometer) plus AERONET sun-photometer and the multi-wavelength lidar plus AERONET sun-photometer configurations in GRASP algorithm. Instead of the

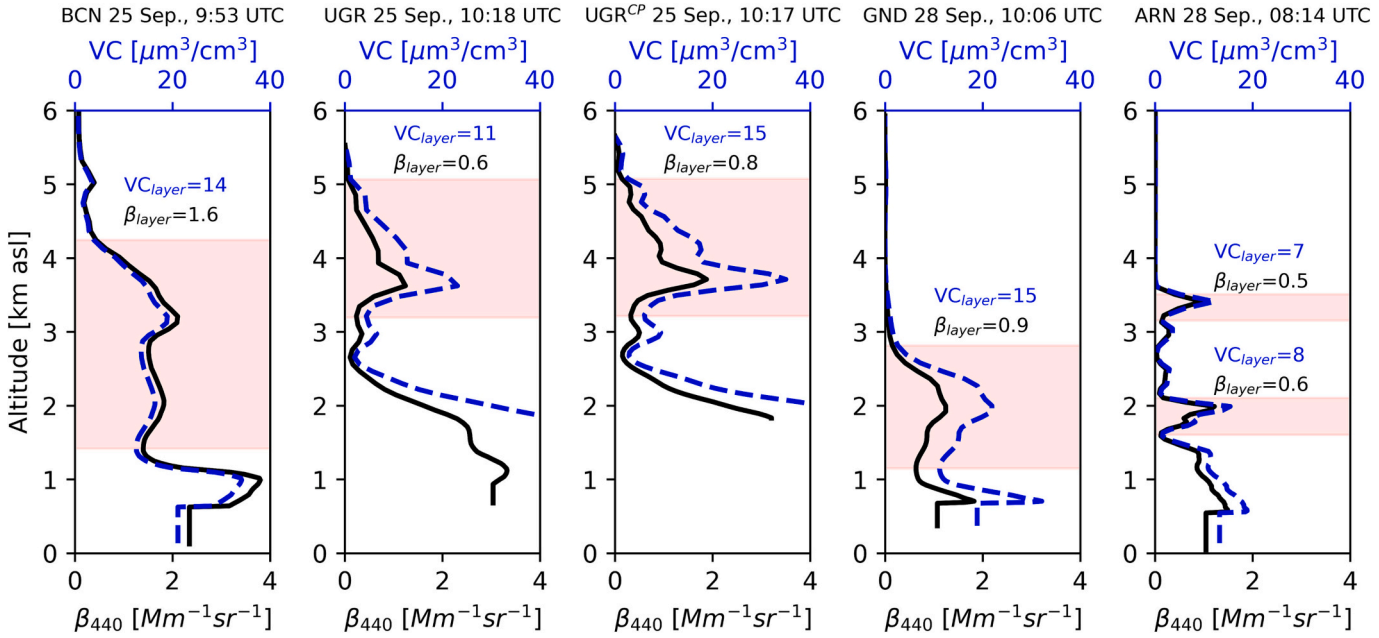

Fig. 11. Optical and microphysical profiles obtained from GRASP retrievals for representative cases of the VA Event I (25–28 September 2021) in the sites where the retrievals are available. The VA layers are highlighted by the shadowed areas and the VC_{layer} and β_{layer} are the layer mean values.

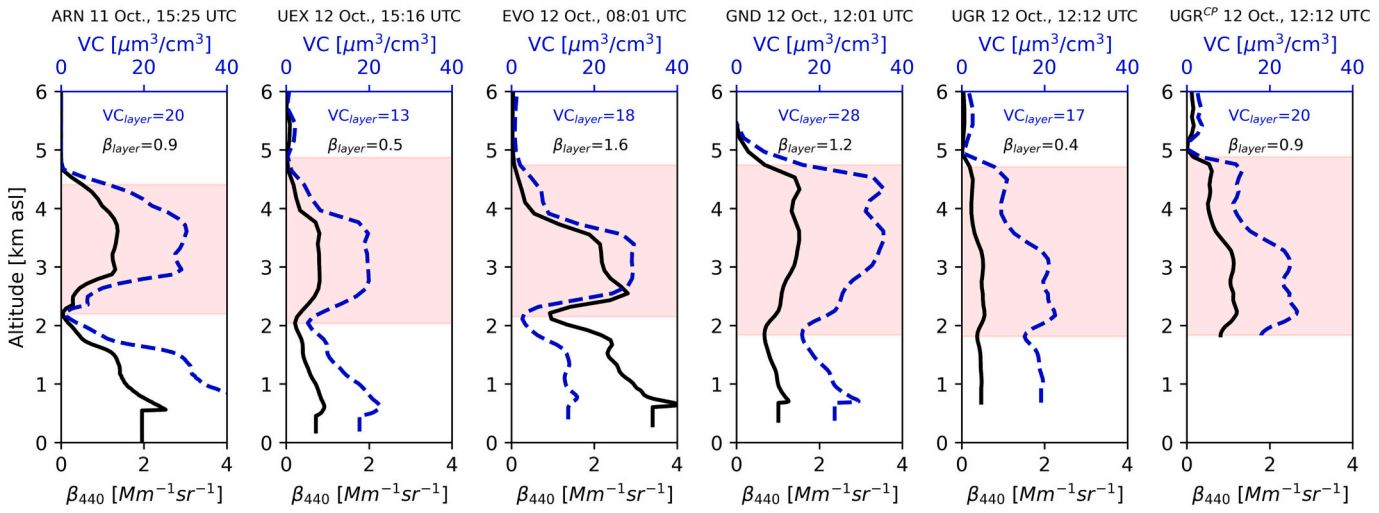

Fig. 12. Optical and microphysical profiles obtained from GRASP retrievals for representative cases of the VA Event II (11–13 October 2021) in the sites where the retrievals are available. The VA layers are highlighted by the shadowed areas and the VC_{layer} and β_{layer} are the layer mean values.

wavelength 532 nm, here the results are presented at 440 nm for comparison purposes, since this wavelength is common to all GRASP configurations used. The results are shown for representative volcanic aerosol cases detected in different stations. The use of GRASP retrievals was restricted to clear sky situations, which limited the availability of data due to the synoptic conditions. For event I (Fig. 11), profiles of β_{440} and VC were available in Cerro-Poyos, Granada and Barcelona sites and data are shown for 25 September. Comparing the different sites, Cerro-Poyos and Granada presented very similar layers that extend from about 3–5 km asl. This similarity is expected due to the proximity of the stations (the ceilometer data used in the retrieval is the same). Despite that, Cerro-Poyos presents higher VC in the layer centre than in Granada. Still, on 25 September, a more extensive layer (1.5–4.2 km asl) was observed in Barcelona station with a maximum VC around 3 km agl. This agrees with the Hysplit backward-trajectories ending in Barcelona at 08:00 UTC (figure not shown) that presented similar patterns at all simulated heights (1–5 km with steps of 0.5 km) to the volcanic aerosol plume observed by TROPOMI (Fig. 3). On 28 September the situation changed, volcanic aerosol layers were observed at lower altitudes (1.1–2.8 km asl) in Guadiana-UGR station, and around 1.6–2.1 km and 3.1–3.5 km asl in El-Arenosillo/Huelva station.

For event II, the selected GRASP retrieved profiles (Fig. 12) showed well defined volcanic aerosol layers at the different sites. Fig. 12 is mainly represented for 12 October, the day of maximum intensity, except for El-Arenosillo/Huelva due to cloud presence. Despite that, a layer defined between 2.2 and 4.4 km asl can be observed at El-Arenosillo/Huelva on 11 October with VC higher than 20 $\mu m^3 cm^{-3}$ in the centre. On 12 October, at Cerro-Poyos, Granada and Guadiana-UGR stations the profiles presented similar upper-level layers with extensions around 1.8–4.9 km. The upper-level layers at Cerro-Poyos and Granada stations presented a maximum VC of around 20 $\mu m^3 cm^{-3}$, while in Guadiana-UGR station these values exceeded the 20 $\mu m^3 cm^{-3}$. The

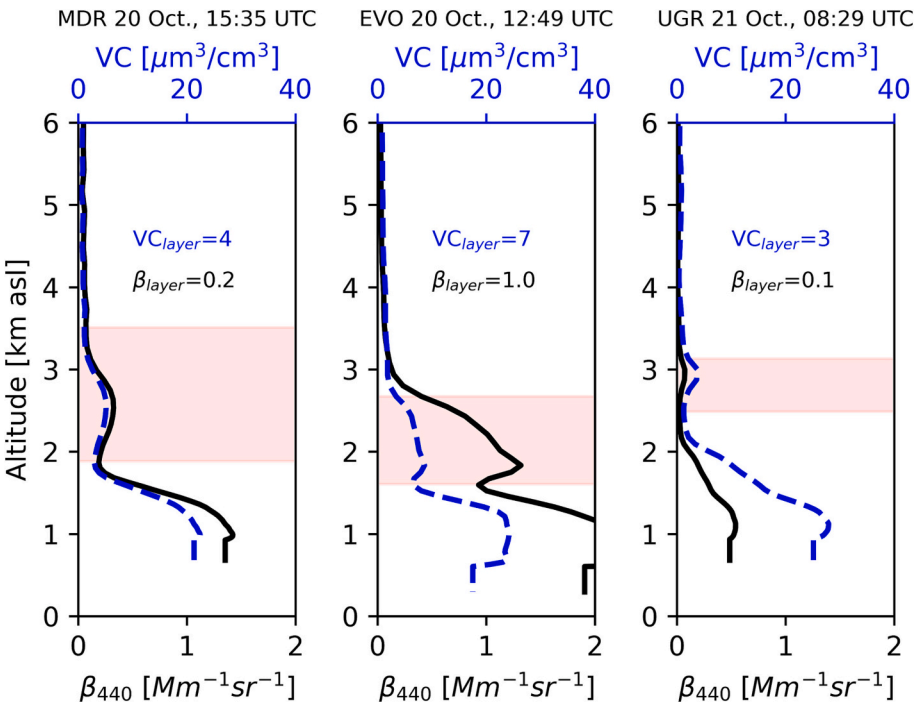

Fig. 13. Optical and microphysical profiles obtained from GRASP retrievals for representative cases of the VA Event III (19–21 October 2021) in the sites where the retrievals are available. The VA layers are highlighted by the shadowed areas and the VC_{layer} and β_{layer} are the layer mean values.

profiles for Évora and Badajoz stations showed upper-level layers extending from about 2–4 km asl. The profiles in Évora during the morning showed higher values of β_{440} and VC (maximum values of 2.8 Mm^{-1} sr^{-1} and 29.6 $\mu m^3 cm^{-3}$, respectively) than in Badajoz (maximum values of 0.8 Mm^{-1} sr^{-1} and 19.9 $\mu m^3 cm^{-3}$, respectively), where the profiles were mostly acquired during the afternoon when the event intensity started to decrease.

For the last event (III), there were only three VA profiles available (Fig. 13) for Madrid, Évora and Granada stations, respectively. The upper-level volcanic aerosol layers were sequentially detected in Évora, later in Madrid and finally in Granada. The volcanic aerosol plume weakened as it moved eastward, with high β_{440} and VC values observed in Évora (maximum values of 1.3 Mm^{-1} sr^{-1} and 8.7 $\mu m^3 cm^{-3}$, respectively) where the layer extended from 1.6 to 2.7 km.

In Évora station, due to the GRASP configuration used (multi-wavelength lidar plus AERONET sun-photometer), it is possible to distinguish between fine and coarse aerosol modes. Fig. 14a shows representative profiles of VC for fine and coarse modes for the event II. During this event, the VC mean values of the fine and coarse modes are 6 ± 5 $\mu m^3 cm^{-3}$ and 12 ± 6 $\mu m^3 cm^{-3}$, respectively, considering all the available GRASP profiles where the volcanic layer was identified. Fig. 14b shows the representative VC for the unique profile of event III in Évora. In this case, VC mean values of 3 $\mu m^3 cm^{-3}$ and 4 $\mu m^3 cm^{-3}$ are obtained for fine and coarse modes, respectively. Although the VC of coarse mode is twice the VC of the fine mode in event II, the lidar observations showed the presence of low depolarizing particles during events II and III (subsection 3.3).

3.4.3. *Aerosol properties in the volcanic layer*

Table 3 shows the volcanic aerosol layer mean values of β_{440} and VC for all GRASP retrievals in each site during the events. For event I, the β_{440} at El-Arenosillo/Huelva and Granada stations were lower than 1.5 Mm^{-1} sr^{-1} with mean values of 0.4 ± 0.3 Mm^{-1} sr^{-1} and 0.35 ± 0.24 Mm^{-1} sr^{-1} respectively. At Cerro-Poyos and Guadiana-UGR stations, with mean values of 1.1 ± 0.7 Mm^{-1} sr^{-1} and 0.9 ± 0.6 Mm^{-1} sr^{-1} respectively, the β_{440} were higher than those observed for El-Arenosillo/Huelva and Granada stations. Barcelona station, represented only by one

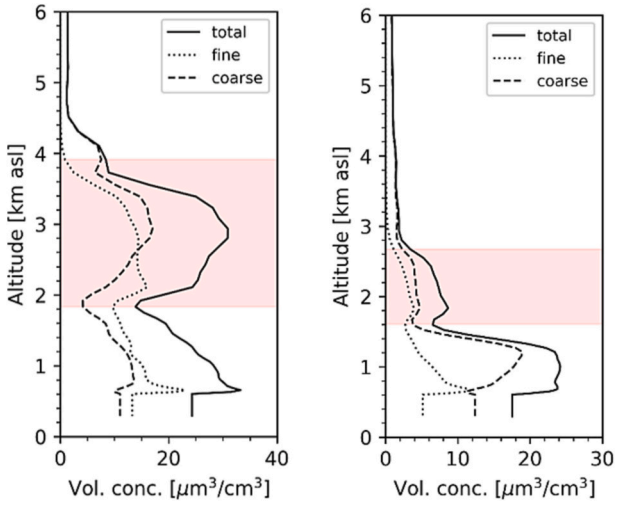

Fig. 14. Particle volume concentration for the different modes from the multi-wavelength Raman lidar plus sun-photometer configuration in GRASP algorithm: (a) 12 October 2021 at 13:29 UTC and (b) 20 October at 12:49 UTC. The volcanic aerosol layers are highlighted by the shadowed areas.

profile (Fig. 11), had a mean β_{440} of 1.6 ± 0.3 Mm^{-1} sr^{-1}. During this event, the VC at El-Arenosillo/Huelva station was always lower than 15.4 $\mu m^3 cm^{-3}$ with a mean value of 5 ± 4 $\mu m^3 cm^{-3}$. The VC at Cerro Poyos (14 ± 7 $\mu m^3 cm^{-3}$), Granada (11 ± 8 $\mu m^3 cm^{-3}$), and Guadiana-UGR (17 ± 10 $\mu m^3 cm^{-3}$) stations present some occurrences around 40 $\mu m^3 cm^{-3}$ although most of the values (Cerro Poyos 89%, Granada 87% and Guadiana-UGR 76%) were between 0 and 20 $\mu m^3 cm^{-3}$. In Barcelona station, the VC had a mean value of 14 ± 3 $\mu m^3 cm^{-3}$. These results suggest changes in the volcanic aerosols as the plume moved. The western station, El-Arenosillo/Huelva, presented the lowest values of VC because the available profiles correspond to 27 and 28 September when the plume started to dissipate, while for all other sites there were profiles

Table 3
Total volume concentration and backscatter coefficient mean values and standard deviation obtained from GRASP algorithm retrievals of the VA layer. The values marked with an * correspond to the unique available profile obtained on the corresponding day.

Site	Event I		Event II		Event III	
	β_{440} [Mm^{-1} sr^{-1}]	VC [$\mu m^3 cm^{-3}$]	β_{440} [Mm^{-1} sr^{-1}]	VC [$\mu m^3 cm^{-3}$]	β_{440} [Mm^{-1} sr^{-1}]	VC [$\mu m^3 cm^{-3}$]
BCN	1.6 ± 0.3*	14 ± 3*	–	–	–	–
MDR	–	–	–	–	0.2 ± 0.1*	4 ± 1*
UEX	–	–	0.5 ± 0.4	11 ± 7	–	–
EVO	–	–	1.7 ± 0.8	19 ± 7	1.0 ± 0.3*	7 ± 1*
GDN	0.9 ± 0.6	17 ± 10	1.0 ± 0.4	27 ± 10	–	–
UGR	0.4 ± 0.2	11 ± 8	0.5 ± 0.3	17 ± 7	0.04 ± 0.02	2 ± 1
UGR^{CP}	1.1 ± 0.7	14 ± 7	1.5 ± 0.6	25 ± 10	–	–
ARN	0.4 ± 0.3	5 ± 4	0.8 ± 0.4	15 ± 7	–	–

for 25 September, the beginning of the event.

For event II, the β_{440} at El-Arenosillo/Huelva, Granada, Guadiana-UGR and Badajoz stations are lower than 2 Mm^{-1} sr^{-1}, while at Cerro-Poyos and Évora stations, there are occurrences for β_{440} larger than 2 Mm^{-1} sr^{-1} (see Table 3). In this event, the VC at El-Arenosillo/Huelva is larger than in event I, with a mean value of 15 ± 7 $\mu m^3 cm^{-3}$. Also, in Cerro-Poyos, Granada and Guadiana-UGR the VC values were larger than in event I with mean values of 25 ± 10 $\mu m^3 cm^{-3}$, 17 ± 7 $\mu m^3 cm^{-3}$ and 27 ± 10 $\mu m^3 cm^{-3}$ respectively. In Évora, the VC are distributed mainly between 5 and 30 $\mu m^3 cm^{-3}$ with a mean value of 19 ± 7 $\mu m^3 cm^{-3}$ while in Badajoz the variation range is between 0 and 15 $\mu m^3 cm^{-3}$ with a mean value of 11 ± 7 $\mu m^3 cm^{-3}$. During event III, the β_{440} and VC are lower with respect to the other two events. Évora with a VC value of 7 ± 1 $\mu m^3 cm^{-3}$, was the station where the VC was larger followed by Madrid (4 ± 1 $\mu m^3 cm^{-3}$) and Granada (2 ± 1 $\mu m^3 cm^{-3}$).

In general, the VC presents higher values in all sites during event II with respect to events I and III. For event I, Barcelona was the station where the highest mean value of VC was obtained, followed by Granada, Cerro-Poyos, Guadiana-UGR and El-Arenosillo/Huelva stations. Note that the VC for Barcelona corresponds to only one measured profile. For event II, Guadiana-UGR was the site with the highest mean value of VC followed by Cerro-Poyos, Évora, Granada, El-Arenosillo/Huelva and Badajoz stations. Previously, it was demonstrated from Raman lidar observations that event II was more intense in terms of AOD_L^{532}, layer thickness and event duration, than event III. The comparison described also confirms that of the three VA events over the IP, event II was in general the most intense in terms of sulphate VC and β_{440}.

Fig. 15 shows the distributions of the AOD at 440 nm (AOD_L^{440}) in the volcanic layer obtained from the GRASP retrievals at the different stations where the plumes were identified during events I and II. In general, the AOD_L^{440} presents more variability during event II at all stations and it is distributed over a larger range of values than during event I. In event I, El-Arenosillo/Huelva presents low AOD_L^{440} with a mean value of 0.007. In this particular case the plumes were identified on 27 and 28 September, at the end of the event when the plumes started to dissipate. On the other hand, in event I, Barcelona presents the highest AOD_L^{440} corresponding to a value of 0.135 obtained from the only profile where the plumes were identified at this station, on 25 September (Fig. 11). In the event II, the AOD_L^{440} varied between 0.062 (at El-Arenosillo/Huelva) and 0.202 (at Guadiana). The variability observed in AOD_L^{440} can be explained by the number of different days/times with plume occurrences and whether the plumes are identified at the beginning, end or during the whole event, since the plume may have different aerosol contents in different days. For instance, in the event I, the maximum values of AOD_L^{440} varied with day from site to site, which is explained by the plume transport described previously in section 3.2. As mentioned before the maximum AOD_L^{440} of the event was obtained for Barcelona on 25 September, a value of 0.135 that contributed to 52% of the AOD_C^{440}. As in Barcelona, the maximum AOD_L^{440} at Cerro-Poyos (0.060 and 25% for AOD_C^{440}) is also on 25 September, but at Guadiana-UGR (0.107 and 52% for AOD_C^{440}), Granada (0.048 and 32% for AOD_C^{440}) and El-Arenosillo/Huelva (0.010 and 9% for AOD_C^{440}) the maximum values are obtained on 28 September (these values can be seen in table S1 of the supplementary material).

In general, during event II the sites at lower latitudes presented the highest AOD values due to the plume transport path. Guadiana-UGR with mean AOD_L^{440} of 0.233 on 12 October was the site that presented the larger mean value of AOD_L^{440} during this event contributing to 52% for the AOD_C^{440}. It was followed by Cerro-Poyos (0.139 and 43% for AOD_C^{440}), Granada (0.136 and 34% for AOD_C^{440}), Évora (0.107 and 42% for AOD_C^{440}), El-Arenosillo/Huelva (0.103 and 21% for AOD_C^{440}) and Badajoz (0.097 and 34% for AOD_C^{440}). The mean layer thickness was also larger during this event at all sites. The obtained mean values of AOD_L^{440} for Évora are comparable to those reported in section 3.3 for AOD_L^{532}

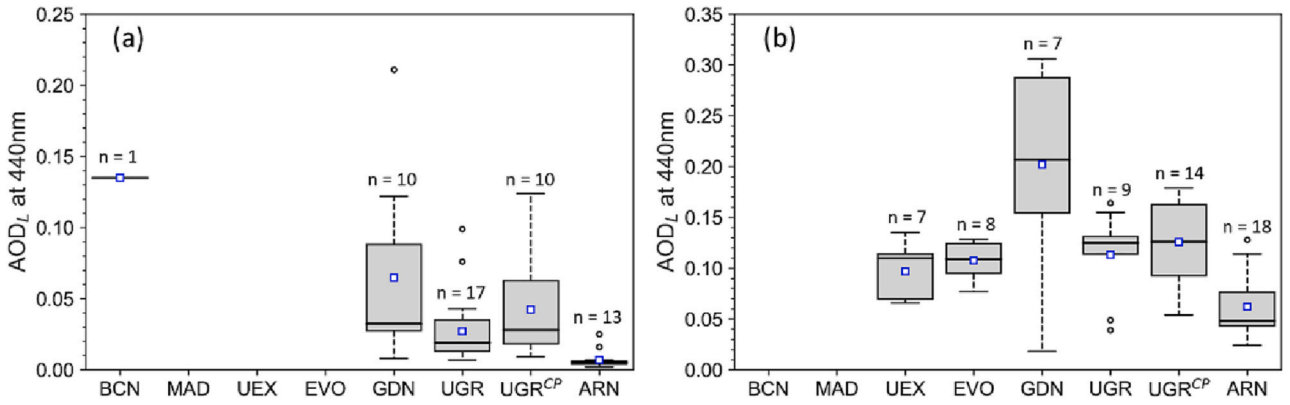

Fig. 15. Volcanic layer aerosol optical depth at the different sites during: (a) event I and (b) event II. The blue square represents the mean value, the black line represents the median and the whiskers show the maximum and minimum values. (For interpretation of the references to colour in this figure legend, the reader is referred to the web version of this article.)

(0.12 ± 0.02) from lidar measurements. The lower AOD_L^{440} were obtained for event III with values of 0.014 at Madrid, 0.003 at Granada and 0.026 at Évora that contributes to 22% for the AOD_C^{440}, followed by Madrid (18% for AOD_C^{440}) and Granada (3% for AOD_C^{440}). In this case, the AOD_L^{440} in Évora station also agrees with the AOD_L^{532} (0.02 ± 0.01) reported in Table 2. These results for event III clearly show the spatio-temporal evolution of the VA plume, which became weak as it moved over the IP crossing Évora, followed by Madrid and Granada until it dissipated (Fig. 3).

4. Conclusions

This work presents the characterization of the spatio-temporal evolution of three volcanic plumes detected in the troposphere over the IP (event I: 25–28 September, event II: 11–13 October and event III: 19–21 October) during the Tajogaite eruptive activity from September to December 2021. The transports are first analysed by using satellite remote sensing data, which show volcanic ash plumes top heights located in the low and middle troposphere distributed horizontally over an area near the volcanic cone. Satellite data also show the presence of SO_2 volcanic plumes over the IP during events I, II and III. These results are corroborated by multi-wavelength Raman lidar measurements (Évora site) of low δ_p and high $\beta\text{-}AE_{532/1064}$ that indicate the presence of fine-mode spherical particles in the atmosphere during events II and III (lidar retrievals were not possible to obtain for event I). The δ_p is relatively constant during event II (0.08 ± 0.02 to 0.09 ± 0.02), and similar to δ_p measured for event III (0.09 ± 0.02). The LR_{532} observed is lower for event III (46 ± 10 sr) than for event II (52 ± 14 sr to 54 ± 15 sr) where significant changes are not observed. This difference in LR_{532} between both events suggests that during the transport the volcanic aerosols may have interacted with aerosols from other sources. The Raman lidar observations also show that event II is more intense in terms of AOD_L^{532}, Δz and event duration (around two days) than event III. The more comprehensive analysis using GRASP at the different sites distributed over the south and southeast of IP shows that, in general, the southernmost sites are those where the highest values of VC and AOD_L^{440} are found, mainly during event II. The VC mean values range between 11 ± 7 $\mu m^3 cm^{-3}$ (Badajoz) and 27 ± 10 $\mu m^3 cm^{-3}$ (Guadiana). Maximum mean values of AOD_L^{440} are obtained for 12 October at all sites varying between 0.097 (Badajoz) and 0.233 (Guadiana), with contributions to the AOD_C^{440} in the range of 21%–52%. The exception is Barcelona where AOD_L^{440} of 0.135 is found in event I. The event I is the second most important in terms of VC, AOD_L^{440} and the number of sites (mainly the southernmost, except Barcelona) where the volcanic plume was detected. The event III is the weakest in terms of VC, AOD_L^{440} and the number of sites (Madrid, Évora and Granada) where the volcanic plume was detected. In event III, the volcanic plume was transported through the Atlantic Ocean crossing the IP in the direction NW-SE, causing Évora to be the first site detecting the plume followed by Madrid and Granada, the southernmost site for this event where the AOD_L^{440} has a value of 0.003 by the end of the event.

Funding

Évora team funded by national funds through FCT - Fundação para a Ciência e Tecnologia, I.P., in the framework of the ICT project with the references UIDB/04683/2020 and UIDP/04683/2020 and by TOMAQAPA (PTDC/CTAMET/29678/2017). The authors acknowledge the GRASP-ACE (Grant agreement ID: 778349), ACTRIS-IMP (Grant agreement ID:871115), ATMO-ACCESS (Grant Agreement ID: 101008004), PROBE (COST Action number: CA18235), HARMONIA (COST Action number: CA21119), EUMETNET through the E-PROFILE program and REALISTIC (Grant agreement ID:101086690) projects. The authors acknowledge the support through ACTRIS-2 under grant agreement no.654109. This work was partially supported by the Spanish national projects PID2019-103886RB-I00/AEI/10.13039/501100011033, INTEGRATYON[3] (PID2020-117825GB-C21 and PID2020-117825GB-C22), ELPIS (PID2020-120015RB-I00), CLARIN (CGL2016-81092-R), ePOLAAR (RTI2018-097864-B-I00), CAMELIA (PID2019-104205GB-C21/AEI/10.13039/501100011033) and ACTRIS-España (CGL2017-90884REDT), by University of Granada Plan Propio through Singular Laboratory (LS2022-1) program, by the Andalusia Autonomous Government projects AEROPRE (P18-RT-3820) and ADAPNE (P20_00136), by the UGR-FEDER projects DEM3TRIOS (A-RNM-430-UGR20) and MOGATRACO (A-RNM-524-UGR20) and partially by the Scientific Units of Excellence Program (grant no. UCE-PP2017-02), and by the R+D+i grant RTI 2018-097332-B-C22 funded by MCIN/AEI/ 10.13039/501100011033/ and "ERDF A Way of Doing Europe". M.-Á. López-Cayuela and C.V. Carvajal-Pérez are supported by the INTA predoctoral contract program.

CRediT authorship contribution statement

V. Salgueiro: Conceptualization, Methodology, Data curation, Formal analysis, Visualization, Writing – original draft, Writing – review & editing. **J.L. Guerrero-Rascado:** Conceptualization, Methodology, Data curation, Formal analysis, Writing – review & editing, Supervision. **M.J. Costa:** Conceptualization, Methodology, Writing – review & editing, Supervision. **R. Román:** Methodology, Data curation, Writing – review & editing. **A. Cazorla:** Writing – review & editing. **A. Serrano:** Data curation, Writing – review & editing. **F. Molero:** Data curation, Writing – review & editing. **M. Sicard:** Data curation, Writing – review & editing. **C. Córdoba-Jabonero:** Data curation, Writing – review & editing. **D. Bortoli:** Data curation, Writing – review & editing, Supervision, Funding acquisition. **A. Comerón:** Writing – review & editing. **F. T. Couto:** Writing – review & editing. **M.Á. López-Cayuela:** Writing – review & editing. **D. Pérez-Ramírez:** Methodology, Writing – review & editing. **M. Potes:** Writing – review & editing. **J.A. Muñiz-Rosado:** Methodology, Data curation, Writing – review & editing. **M.A. Obregón:** Writing – review & editing. **R. Barragán:** Writing – review & editing. **D.C.F.S. Oliveira:** Writing – review & editing. **J. Abril-Gago:** Writing – review & editing. **R. González:** Writing – review & editing. **C. Gíl-Díaz:** Writing – review & editing. **I. Foyo-Moreno:** Writing – review & editing. **C. Muñoz-Porcar:** Writing – review & editing. **M.J. Granados-Muñoz:** Writing – review & editing. **A. Rodríguez-Gómez:** Writing – review & editing. **M. Herreras-Giralda:** Writing – review & editing. **J.A. Bravo-Aranda:** Writing – review & editing. **C.V. Carvajal-Pérez:** Writing – review & editing. **A. Barreto:** Writing – review & editing. **L. Alados-Arboledas:** Writing – review & editing.

Declaration of Competing Interest

The authors declare that they have no known competing financial interests or personal relationships that could have appeared to influence the work reported in this paper.

Data availability

Data will be made available on request.

Acknowledgements

The authors acknowledge the use of GRASP inversion algorithm software (http://www.grasp-open.com) in this work. The authors also acknowledge the virtual mobility grant (E-COST-GRANT-CA18235-508df2c9) funded by the PROBE Cost Action. C. Córdoba-Jabonero, M.Á. López-Cayuela and C.V. Carvajal-Pérez thank the PIs of the AERONET and MPLNET El Arenosillo/Huelva site and its technical staff for maintenance support. The MPLNET project is funded by the NASA Radiation Sciences Program and Earth Observing System.

Appendix A. Supplementary data

Supplementary data to this article can be found online at https://doi.org/10.1016/j.rse.2023.113684.

References

Althausen, D., Engelmann, R., Baars, H., Heese, B., Ansmann, A., Müller, D., Komppula, M., 2009. Portable raman lidar pollyxt for automated profiling of aerosol backscatter, extinction, and depolarization. J. Atmos. Ocean. Technol. 26, 2366–2378. https://doi.org/10.1175/2009JTECHA1304.1.

Ansmann, A., Tesche, M., Seifert, P., Groß, S., Freudenthaler, V., Apituley, A., Wilson, K. M., Serikov, I., Linné, H., Heinold, B., Hiebsch, A., Schnell, F., Schmidt, J., Mattis, I., Wandinger, U., Wiegner, M., 2011. Ash and fine-mode particle mass profiles from EARLINET-AERONET observations over Central Europe after the eruptions of the Eyjafjallajökull volcano in 2010. J. Geophys. Res. Atmos. 116, 1–15. https://doi.org/10.1029/2010JD015567.

Ansmann, A., Wandinger, U., Riebesell, M., Weitkamp, C., Michaelis, W., 1992. Independent measurement of extinction and backscatter profiles in cirrus clouds by using a combined raman elastic-backscatter lidar. Appl. Opt. 31, 7113–7131. https://doi.org/10.1364/AO.31.007113.

Arason, P., Petersen, G.N., Bjornsson, H., 2011. Observations of the altitude of the volcanic plume during the eruption of Eyjafjallajökull, April-may 2010. Earth Syst. Sci. Data 3, 9–17. https://doi.org/10.5194/essd-3-9-2011.

Bazo, E., Granados-Muñoz, M.J., Román, R., Bravo-Aranda, J.A., Cazorla, A., Valenzuela, A., González, R., Olmo, F.J., Alados-Arboledas, L., 2023. Evaluation of the vertically-resolved aerosol radiative effect on shortwave and longwave ranges using sun-sky photometer and ceilometer measurements. Atmos. Res. 282 https://doi.org/10.1016/j.atmosres.2022.106517.

Benavent-Oltra, J.A., Casquero-Vera, J.A., Román, R., Lyamani, H., Pérez-Ramírez, D., Granados-Munõz, M.J., Herrera, M., Cazorla, A., Titos, G., Ortiz-Amezcua, P., Bedoya-Velásquez, A.E., De Arruda Moreira, G., Pérez, N., Alastuey, A., Dubovik, O., Guerrero-Rascado, J.L., Olmo-Reyes, F.J., Alados-Arboledas, L., 2021. Overview of the SLOPE i and II campaigns: aerosol properties retrieved with lidar and sun-sky photometer measurements. Atmos. Chem. Phys. 21, 9269–9287. https://doi.org/10.5194/acp-21-9269-2021.

Benavent-Oltra, J.A., Román, R., Andrés Casquero-Vera, J., Pérez-Ramírez, D., Lyamani, H., Ortiz-Amezcua, P., Bedoya-Velásquez, A.E., De Arruda Moreira, G., Barreto, Á., Lopatin, A., Fuertes, D., Herrera, M., Torres, B., Dubovik, O., Luis Guerrero-Rascado, J., Goloub, P., Olmo-Reyes, F.J., Alados-Arboledas, L., 2019. Different strategies to retrieve aerosol properties at night-time with the GRASP algorithm. Atmos. Chem. Phys. 19, 14149–14171. https://doi.org/10.5194/acp-19-14149-2019.

Benavent-Oltra, J.A., Román, R., Granados-Munõz, M.J., Pérez-Ramírez, D., Ortiz-Amezcua, P., Denjean, C., Lopatin, A., Lyamani, H., Torres, B., Guerrero-Rascado, J. L., Fuertes, D., Dubovik, O., Chaikovsky, A., Olmo, F.J., Mallet, M., Alados-Arboledas, L., 2017. Comparative assessment of GRASP algorithm for a dust event over Granada (Spain) during ChArMEx-ADRIMED 2013 campaign. Atmos. Meas. Tech. 10, 4439–4457. https://doi.org/10.5194/amt-10-4439-2017.

Campbell, J.R., Hlavka, D.L., Welton, E.J., Flynn, C.J., Turner, D.D., Spinhirne, J.D., Stanley, S., Hwang, I.H., 2002. Full-time, eye-safe cloud and aerosol lidar observation at atmospheric radiation measurement program sites: instruments and data processing. J. Atmos. Ocean. Technol. 19, 431–442. https://doi.org/10.1175/1520-0426(2002)019<0431:FTESCA>2.0.CO;2.

Cazorla, A., Andrés Casquero-Vera, J., Román, R., Luis Guerrero-Rascado, J., Toledano, C., Cachorro, V.E., Orza, J.A.G., Cancillo, M.L., Serrano, A., Titos, G., Pandolfi, M., Alastuey, A., Hanrieder, N., Alados-Arboledas, L., 2017. Near-real-time processing of a ceilometer network assisted with sun-photometer data: monitoring a dust outbreak over the Iberian Peninsula. Atmos. Chem. Phys. 17, 11861–11876. https://doi.org/10.5194/acp-17-11861-2017.

Colette, A., Favez, O., Meleux, F., Chiappini, L., Haeffelin, M., Morille, Y., Malherbe, L., Papin, A., Bessagnet, B., Menut, L., Leoz, E., Rouïl, L., 2011. Assessing in near real time the impact of the april 2010 Eyjafjallajökull ash plume on air quality. Atmos. Environ. 45, 1217–1221. https://doi.org/10.1016/j.atmosenv.2010.09.064.

Córdoba-Jabonero, C., Ansmann, A., Jiménez, C., Baars, H., López-Cayuela, M.Á., Engelmann, R., 2021. Experimental assessment of a micro-pulse lidar system in comparison with reference lidar measurements for aerosol optical properties retrieval. Atmos. Meas. Tech. 14, 5225–5239. https://doi.org/10.5194/amt-14-5225-2021.

Córdoba-Jabonero, C., Sicard, M., Ansmann, A., Del Águila, A., Baars, H., 2018. Separation of the optical and mass features of particle components in different aerosol mixtures by using POLIPHON retrievals in synergy with continuous polarized micro-pulse lidar (P-MPL) measurements. Atmos. Meas. Tech. 11, 4775–4795. https://doi.org/10.5194/amt-11-4775-2018.

Córdoba-Jabonero, C., Sicard, M., Barreto, A., Toledano, T., López-Cayuela, M.Á., Gil-Díaz, C., García, O., Carvajal-Pérez, C.V., Comerón, A., Ramos, R., Muñoz-Porcar, C., Rodríguez-Gómez, A., 2023. Fresh volcanic aerosols injected in the atmosphere during the volcano eruptive activity at the cumbre vieja area (La Palma, Canary Islands): temporal evolution and vertical impact. Atmos. Environ. 300, 119667 https://doi.org/10.1016/j.atmosenv.2023.119667.

Córdoba-Jabonero, C., Sicard, M., del Águila, A., Jiménez, M., Zorzano, M.P., 2019. Performance of a dust model to predict the vertical mass concentration of an extreme saharan dust event in the Iberian Peninsula: comparison with continuous, elastic, polarization-sensitive lidars. Atmos. Environ. 214, 116828 https://doi.org/10.1016/j.atmosenv.2019.116828.

Corradini, S., Merucci, L., Prata, A.J., 2009. Retrieval of SO2 from thermal infrared satellite measurements: correction procedures for the effects of volcanic ash. Atmos. Meas. Tech. 2, 177–191. https://doi.org/10.5194/amt-2-177-2009.

Corradini, S., Merucci, L., Prata, A.J., Piscini, A., 2010. Volcanic ash and SO2 in the 2008 kasatochi eruption: retrievals comparison from different IR satellite sensors. J. Geophys. Res. Atmos. 115, 1–10. https://doi.org/10.1029/2009JD013634.

Corradini, S., Spinetti, C., Carboni, E., Tirelli, C., Buongiorno, M.F., Pugnaghi, S., Gangale, G., 2008. Mt. Etna tropospheric ash retrieval and sensitivity analysis using moderate resolution imaging spectroradiometer measurements. J. Appl. Remote. Sens. 2 (1), 023550 https://doi.org/10.1117/1.3046674.

D'Amico, G., Amodeo, A., Mattis, I., Freudenthaler, V., Pappalardo, G., 2016. EARLINET single calculus chain-technical andndash; part 1: pre-processing of raw lidar data. Atmos. Meas. Tech. 9, 491–507. https://doi.org/10.5194/amt-9-491-2016.

Dubovik, O., Fuertes, D., Litvinov, P., Lopatin, A., Lapyonok, T., Doubovik, I., Xu, F., Ducos, F., Chen, C., Torres, B., Derimian, Y., Li, L., Herreras-Giralda, M., Herrera, M., Karol, Y., Matar, C., Schuster, G.L., Espinosa, R., Puthukkudy, A., Li, Z., Fischer, J., Preusker, R., Cuesta, J., Kreuter, A., Cede, A., Aspetsberger, M., Marth, D., Bindreiter, L., Hangler, A., Lanzinger, V., Holter, C., Federspiel, C., 2021. A comprehensive description of multi-term LSM for applying multiple a priori constraints in problems of atmospheric remote sensing: GRASP algorithm, concept, and applications. Front. Remote Sens. 2, 1–52. https://doi.org/10.3389/frsen.2021.706851.

Dubovik, O., King, M.D., 2000. A flexible inversion algorithm for retrieval of aerosol optical properties from sun and sky radiance measurements. J. Geophys. Res. Atmos. 105, 20673–20696. https://doi.org/10.1029/2000JD900282.

Dubovik, O., Lapyonok, T., Litvinov, P., Herman, M., Fuertes, D., Ducos, F., Torres, B., Derimian, Y., Huang, X., Lopatin, A., Chaikovsky, A., Michael Aspetsberger, M., Federspiel, C., 2014. GRASP: a versatile algorithm for characterizing the atmosphere. SPIE Newsroom. 25, 151–158. https://doi.org/10.1117/%0A2.1201408.005558.

Dubovik, O., Sinyuk, A., Lapyonok, T., Holben, B.N., Mishchenko, M., Yang, P., Eck, T.F., Volten, H., Muñoz, O., Veihelmann, B., van der Zande, W.J., Leon, J.F., Sorokin, M., Slutsker, I., 2006. Application of spheroid models to account for aerosol particle nonsphericity in remote sensing of desert dust. J. Geophys. Res. Atmos. 111, 1–34. https://doi.org/10.1029/2005JD006619.

Dubuisson, P., Herbin, H., Minvielle, F., Thieuleux, F., Parol, F., Pelon, J., Systems, D., Systems, D., 2013. Remote sensing of volcanic ash plumes from thermal infrared: a case study analysis from SEVIRI, MODIS and IASI instruments. Atmos. Meas. Tech. 6, 2793–2828. https://doi.org/10.5194/amtd-6-2793-2013.

Fernald, F.G., Herman, B.M., Reagan, J.A., 1972. Determination of aerosol height distributions by lidar. J. Appl. Meteorol. 11, 482–489. https://doi.org/10.1175/1520-0450(1972)011<0482:DOAHDB>2.0.CO;2.

Fernald, G.F., 1984. Analysis of atmospheric lidar observations: some comments. Appl. Opt. 23, 652–653. https://doi.org/10.1364/AO.23.000652.

Flamant, C., Pelon, J., Flamant, P.H., Durand, P., 1997. Lidar determination of the entrainment zone thickness at the top of the unstable marine atmospheric boundary layer. Bound.-Layer Meteorol. 83, 247–284. https://doi.org/10.1023/A:1000258318944.

Flynn, C.J., Mendoza, A., Zheng, Y., Mathur, S., 2007. Novel polarization-sensitive micropulse lidar measurement technique. Opt. Express 15, 2785. https://doi.org/10.1364/oe.15.002785.

Fuertes, D., Toledano, C., González, R., Berjón, A., Torres, B., Cachorro, V.E., De Frutos, Á.M., 2018. CÆLIS: software for assimilation, management and processing data of an atmospheric measurement network. Geosci. Instrum. Methods Data Syst. 7, 67–81. https://doi.org/10.5194/gi-7-67-2018.

Gassó, S., 2008. Satellite observations of the impact of weak volcanic activity on marine clouds. J. Geophys. Res. 113, 1–14. https://doi.org/10.1029/2007jd009106.

Giles, D.M., Sinyuk, A., Sorokin, M.G., Schafer, J.S., Smirnov, A., Slutsker, I., Eck, T.F., Holben, B.N., Lewis, J.R., Campbell, J.R., Welton, E.J., Korkin, S.V., Lyapustin, A.I., 2019. Advancements in the aerosol robotic network (AERONET) version 3 database - automated near-real-time quality control algorithm with improved cloud screening for sun photometer aerosol optical depth (AOD) measurements. Atmos. Meas. Tech. 12, 169–209. https://doi.org/10.5194/amt-12-169-2019.

González, R., Toledano, C., Román, R., Fuertes, D., Berjón, A., Mateos, D., Guirado-Fuentes, C., Velasco-Merino, C., Antuña-Sánchez, J.C., Calle, A., Cachorro, V.E., De Frutos, Á.M., 2020. Daytime and nighttime aerosol optical depth implementation in CÆLIS. Geosci. Instrum. Methods Data Syst. 9, 417–433. https://doi.org/10.5194/gi-9-417-2020.

Global Volcanism Program, 2022. Report on La Palma (Spain). Available online at. In: Bennis, K.L., Venzke, E. (Eds.), Bulletin of the Global Volcanism Network, 47:2. Smithsonian Institution (last access on 8 July, 2022). https://volcano.si.edu/showreport.cfm?doi=10.5479/si.GVP.BGVN202202-383010.

Global Volcanism Program, 2021. Report on La Palma (Spain). In: Sennert, S.K. (Ed.), Weekly Volcanic Activity Report, 27 October-2 November 2021. Smithsonian Institution and US-Geological Survey.

Granados-Muñoz, M.J., Navas-Guzmán, F., Bravo-Aranda, J.A., Guerrero-Rascado, J.L., Lyamani, H., Valenzuela, A., Titos, G., Fernández-Gálvez, J., Alados-Arboledas, L., 2015. Hygroscopic growth of atmospheric aerosol particles based on active remote sensing and radiosounding measurements: selected cases in southeastern Spain. Atmos. Meas. Tech. 8, 705–718. https://doi.org/10.5194/amt-8-705-2015.

Heese, B., Flentje, H., Althausen, D., Ansmann, A., Frey, S., 2010. Ceilometer lidar comparison: backscatter coefficient retrieval and signal-to-noise ratio determination. Atmos. Meas. Tech. 3, 1763–1770. https://doi.org/10.5194/amt-3-1763-2010.

Herreras, M., Román, R., Cazorla, A., Toledano, C., Lyamani, H., Torres, B., Cachorro, V. E., Olmo, F.J., Alados-Arboledas, L., de Frutos, A.M., 2019. Evaluation of retrieved aerosol extinction profiles using as reference the aerosol optical depth differences between various heights. Atmos. Res. 230, 104625 https://doi.org/10.1016/j.atmosres.2019.104625.

Hervo, M., Quennehen, B., Kristiansen, N.I., Boulon, J., Stohl, A., Fréville, P., Pichon, J. M., Picard, D., Labazuy, P., Gouhier, M., Roger, J.C., Colomb, A., Schwarzenboeck, A., Sellegri, K., 2012. Physical and optical properties of 2010 Eyjafjallajökull volcanic eruption aerosol: ground-based, lidar and airborne measurements in France. Atmos. Chem. Phys. 12, 1721–1736. https://doi.org/10.5194/acp-12-1721-2012.

Holben, B.N., Eck, T.F., Slutsker, I., Tanré, D., Buis, J.P., Setzer, A., Vermote, E., Reagan, J.A., Kaufman, Y.J., Nakajima, T., Lavenu, F., Jankowiak, I., Smirnov, A., 1998. AERONET - a federated instrument network and data archive for aerosol characterization. Remote Sens. Environ. 66, 1–16. https://doi.org/10.1016/S0034-4257(98)00031-5.

Nacional, Instituto Geográfico, 2022. Available online at. https://www.ign.es/web/resources/volcanologia/html/CA_noticias_2021.html (accessed on 8 July 2022).

Kearney, C.S., Watson, I.M., 2009. Correcting satellite-based infrared sulfur dioxide retrievals for the presence of silicate ash. J. Geophys. Res. Atmos. 114, 1–12. https://doi.org/10.1029/2008JD011407.

Klett, J., 1985. Lidar inversion with variable backscatter/extinction ratios title. Appl. Opt. 24, 1638–1643. https://doi.org/10.1364/AO.24.001638.

Klett, J.D., 1981. Stable analytical inversion solution for processing lidar returns. Appl. Opt. 20, 211–220. https://doi.org/10.1364/AO.20.000211.

Kokkalis, P., Papayannis, A., Amiridis, V., Mamouri, R.E., Veselovskii, I., Kolgotin, A., Tsaknakis, G., Kristiansen, N.I., Stohl, A., Mona, L., 2013. Optical, microphysical, mass and geometrical properties of aged volcanic particles observed over Athens, Greece, during the Eyjafjallajökull eruption in april 2010 through synergy of raman lidar and sunphotometer measurements. Atmos. Chem. Phys. 13, 9303–9320. https://doi.org/10.5194/acp-13-9303-2013.

Lopatin, A., Dubovik, O., Chaikovsky, A., Goloub, P., Lapyonok, T., Tanré, D., Litvinov, P., 2013. Enhancement of aerosol characterization using synergy of lidar and sun-photometer coincident observations: the GARRLiC algorithm. Atmos. Meas. Tech. 6, 2065–2088. https://doi.org/10.5194/amt-6-2065-2013.

Lopatin, A., Dubovik, O., Fuertes, D., Stenchikov, G., Lapyonok, T., Veselovskii, I., Wienhold, F.G., Shevchenko, I., Hu, Q., Parajuli, S., 2021. Synergy processing of diverse ground-based remote sensing and in situ data using the GRASP algorithm: applications to radiometer, lidar and radiosonde observations. Atmos. Meas. Tech. 14, 2575–2614. https://doi.org/10.5194/amt-14-2575-2021.

Lopes, F.J.S., Silva, J.J., Marrero, J.C.A., Taha, G., Landulfo, E., 2019. Synergetic aerosol layer observation after the 2015 Calbuco volcanic eruption event. Remote Sens. 11, 1–22. https://doi.org/10.3390/rs11020195.

López-Cayuela, M.A., Córdoba-Jabonero, C., Bermejo-Pantaleón, D., Sicard, M., Salgueiro, V., Molero, F., Carvajal-Pérez, C.V., Granados-Muñoz, M.J., Comerón, A., Couto, F.T., Barragán, R., Zorzano, M.-P., Bravo-Aranda, J.A., Muñoz-Porcar, C., Costa, M.J., Artíñano, B., Rodríguez-Gómez, A., Bortoli, D., Pujadas, M., Abril-Gago, J., Alados-Arboledas, L., Guerrero-Rascado, J.L., 2023. Vertical characterization of fine and coarse dust particles during an intense Saharan dust outbreak over the Iberian Peninsula in springtime 2021. Atmos. Chem. Phys. 23 (1), 143–161. https://doi.org/10.5194/acp-23-143-2023.

López-Cayuela, M.Á., Herrera, M.E., Córdoba-Jabonero, C., Pérez-Ramírez, D., Carvajal-Pérez, C.V., Dubovik, O., Guerrero-Rascado, J.L., 2022. Retrieval of aged biomass-burning aerosol properties by using GRASP code in synergy with polarized micro-pulse. Remote Sens. 14, 1–21. https://doi.org/10.3390/rs14153619.

López-Cayuela, M.Á., Herreras-Giralda, M., Córdoba-Jabonero, C., Lopatin, A., Dubovik, O., Guerrero-Rascado, J.L., 2021. Vertical assessment of the mineral dust optical and microphysical properties as retrieved from the synergy between polarized micro-pulse lidar and sun/sky photometer observations using GRASP code. Atmos. Res. 264 https://doi.org/10.1016/j.atmosres.2021.105818.

Lufft, 2021. Lufft CHM 15k Ceilometer User Manual. R18, February 2021.

Mattis, I., D'Amico, G., Baars, H., Amodeo, A., Madonna, F., Iarlori, M., 2016. EARLINET single calculus chain - technical - part 2: calculation of optical products. Atmos. Meas. Tech. 9, 3009–3029. https://doi.org/10.5194/amt-9-3009-2016.

Mattis, I., Siefert, P., Müller, D., Tesche, M., Hiebsch, A., Kanitz, T., Schmidt, J., Finger, F., Wandinger, U., Ansmann, A., 2010. Volcanic aerosol layers observed with multiwavelength Raman lidar over Central Europe in 2008–2009. J. Geophys. Res. Atmos. 115, 1–9. https://doi.org/10.1029/2009JD013472.

Millán, L., Santee, M.L., Lambert, A., Livesey, N.J., Werner, F., Schwartz, M.J., Pumphrey, H.C., Manney, G.L., Wang, Y., Su, H., Wu, L., Read, W.G., Froidevaux, L., 2022. The hunga Tonga-hunga ha ' apai hydration of the stratosphere. Geophys. Res. Lett. 49, 1–16. https://doi.org/10.1029/2022GL099381.

Minnis, P., Harrison, E.F., Stowe, L.L., Gibson, G.G., Denn, F.M., Doelling, D.R., Smith, W.L., 1993. Radiative climate forcing by the mount pinatubo eruption. Science 259, 1411–1415. https://doi.org/10.1126/science.259.5100.1411.

Molero, F., Pujadas, M., Artíñano, B., 2020. Study of the effect of aerosol vertical profile on microphysical properties using grasp code with sun/sky photometer and multiwavelength lidar measurements. Remote Sens. 12, 1–17. https://doi.org/10.3390/rs12244072.

Mona, L., Amodeo, A., D'Amico, G., Giunta, A., Madonna, F., Pappalardo, G., 2012. Multi-wavelength raman lidar observations of the Eyjafjallajökull volcanic cloud over Potenza, southern Italy. Atmos. Chem. Phys. 12, 2229–2244. https://doi.org/10.5194/acp-12-2229-2012.

Navas-Guzmán, F., Müller, D., Bravo-Aranda, J.A., Guerrero-Rascado, J.L., Granados-Muñoz, M.J., Pérez-Ramírez, D., Olmo, F.J., Alados-Arboledas, L., 2013. Eruption of the Eyjafjallajökull volcano in spring 2010: multiwavelength raman lidar measurements of sulphate particles in the lower troposphere. J. Geophys. Res. Atmos. 118, 1804–1813. https://doi.org/10.1002/jgrd.50116.

Newhall, C.G., Self, S., 1982. The volcanic explosivity index (VEI) an estimate of explosive magnitude for historical volcanism. J. Geophys. Res. Oceans 87 (C2), 1231–1238. https://doi.org/10.1029/JC087iC02p01231.

Papayannis, A., Balis, D., Bais, A., Van Der Bergh, H., Calpini, B., Durieux, E., Fiorani, L., Jaquet, L., Ziomas, I., Zerefos, C.S., 1998. Role of urban and suburban aerosols on solar UV radiation over Athens, Greece. Atmos. Environ. 32, 2193–2201. https://doi.org/10.1016/S1352-2310(97)00411-1.

Papayannis, A., Mamouri, R.E., Amiridis, V., Giannakaki, E., Veselovskii, I., Kokkalis, P., Tsaknakis, G., Balis, D., Kristiansen, N.I., Stohl, A., Korenskiy, M., Allakhverdiev, K., Huseyinoglu, M.F., Baykara, T., 2012. Optical properties and vertical extension of aged ash layers over the eastern Mediterranean as observed by raman lidars during the Eyjafjallajökull eruption in may 2010. Atmos. Environ. 48, 56–65. https://doi.org/10.1016/j.atmosenv.2011.08.037.

Pappalardo, G., Amodeo, A., Apituley, A., Comeron, A., Freudenthaler, V., Linné, H., Ansmann, A., Bösenberg, J., D'Amico, G., Mattis, I., Mona, L., Wandinger, U., Amiridis, V., Alados-Arboledas, L., Nicolae, D., Wiegner, M., 2014. EARLINET: towards an advanced sustainable european aerosol lidar network. Atmos. Meas. Tech. 7, 2389–2409. https://doi.org/10.5194/amt-7-2389-2014.

Perez-Ramirez, D., Whiteman, D.N., Veselovskii, I., Ferrare, R., Titos, G., Granados-Munoz, M.J., Sanchez-Hernandez, G., Navas-Guzman, F., 2021. Spatiotemporal changes in aerosol properties by hygroscopic growth and impacts on radiative forcing and heating rates during DISCOVER-AQ 2011. Atmos. Chem. Phys. 21, 12021–12048. https://doi.org/10.5194/acp-21-12021-2021.

PEVOLCA, 2021. Scientific Committee Report 25/12/2021. Available online at. In: Actualización de la actividad volcánica en Cumbre Vieja (La Palma) (accessed on 11 October 2022). https://www3.gobiernodecanarias.org/noticias/wp-content/uploads/2021/12/251221-INFORME-Comité-Científico-PDF.pdf.

Picchiani, M., Chini, M., Corradini, S., Merucci, L., Sellitto, P., Del Frate, F., Stramondo, S., 2011. Volcanic ash detection and retrievals using MODIS data by means of neural networks. Atmos. Meas. Tech. 4, 2619–2631. https://doi.org/10.5194/amt-4-2619-2011.

Prata, A.J., 1989. Observations of volcanic ash clouds in the 10–12 μm window using AVHRR/2 data. Int. J. Remote Sens. 10 (4–5), 751–761. https://doi.org/10.1080/01431168908903916.

Prata, A.J., Prata, A.T., 2012. Eyjafjallajökull volcanic ash concentrations determined using spin enhanced visible and infrared imager measurements. J. Geophys. Res. Atmos. 117, 1–24. https://doi.org/10.1029/2011JD016800.

Prata, A.T., Young, S.A., Siems, S.T., Manton, M.J., 2017. Lidar ratios of stratospheric volcanic ash and sulfate aerosols retrieved from CALIOP measurements. Atmos. Chem. Phys. 17, 8599–8618. https://doi.org/10.5194/acp-17-8599-2017.

Preißler, J., Wagner, F., Pereira, S.N., Guerrero-Rascado, J.L., 2011. Multi-instrumental observation of an exceptionally strong saharan dust outbreak over Portugal. J. Geophys. Res. Atmos. 116, 1–12. https://doi.org/10.1029/2011JD016527.

Robock, A., 2000. Volcanic eruptions and climate. Rev. Geophys. 191–219.

Román, R., Benavent-Oltra, J.A., Casquero-Vera, J.A., Lopatin, A., Cazorla, A., Lyamani, H., Denjean, C., Fuertes, D., Pérez-Ramírez, D., Torres, B., Toledano, C., Dubovik, O., Cachorro, V.E., de Frutos, A.M., Olmo, F.J., Alados-Arboledas, L., 2018. Retrieval of aerosol profiles combining sunphotometer and ceilometer measurements in GRASP code. Atmos. Res. 204, 161–177. https://doi.org/10.1016/j.atmosres.2018.01.021.

Román, R., González, R., Cazorla, A., Herreras-Giralda, M., Antuña-Sánchez, J., Toledano, C., 2021. CAECENET: columnar and vertically-resolved aerosol products in near-real-time joining Sun/Sky photometer and ceilometer measurement networks. In: European Lidar Conference. Granada.

Salgueiro, V., Costa, M.J., Guerrero-Rascado, J.L., Couto, F.T., Bortoli, D., 2021. Characterization of forest fire and saharan desert dust aerosols over South-Western Europe using a multi-wavelength raman lidar and sun-photometer. Atmos. Environ. 252 https://doi.org/10.1016/j.atmosenv.2021.118346.

Sannino, A., Amoruso, S., Damiano, R., Scollo, S., Sellitto, P., Boselli, A., 2022. Optical and microphysical characterization of atmospheric aerosol in the Central Mediterranean during simultaneous volcanic ash and desert dust transport events. Atmos. Res. 271, 106099 https://doi.org/10.1016/j.atmosres.2022.106099.

Sawamura, P., Vernier, J.P., Barnes, J.E., Berkoff, T.A., Welton, E.J., Alados-Arboledas, L., Navas-Guzmán, F., Pappalardo, G., Mona, L., Madonna, F., Lange, D., Sicard, M., Godin-Beekmann, S., Payen, G., Wang, Z., Hu, S., Tripathi, S.N., Cordoba-Jabonero, C., Hoff, R.M., 2012. Stratospheric AOD after the 2011 eruption of nabro volcano measured by lidars over the northern hemisphere. Environ. Res. Lett. 7 https://doi.org/10.1088/1748-9326/7/3/034013.

Sears, T.M., Thomas, G.E., Carboni, E., Smith, A.J.A., Grainger, R.G., 2013. SO2 as a possible proxy for volcanic ash in aviation hazard avoidance. J. Geophys. Res. Atmos. 118, 5698–5709. https://doi.org/10.1002/jgrd.50505.

Sentinel, 2021. S5P Mission Performance Centre Sulphur Dioxide [L2_SO2_] Readme. Available at (last access on 21 September 2022). https://sentinels.copernicus.eu/web/sentinel/user-guides/sentinel-5p-tropomi/document-library/.

Sicard, M., Córdoba-Jabonero, C., Barreto, A., Welton, E.J., Gil-Díaz, C., Carvajal-Pérez, C.V., Comerón, A., García, O., García, R., López-Cayuela, M.-Á., Muñoz-Porcar, C., Prats, N., Ramos, R., Rodríguez-Gómez, A., Toledano, C., Torres, C., 2022. Volcanic eruption of cumbre vieja, La Palma, Spain: a first insight to the particulate matter injected in the troposphere. Remote Sens. 14, 2470. https://doi.org/10.3390/rs14102470.

Sicard, M., Guerrero-Rascado, J.L., Navas-Guzmán, F., Preißler, J., Molero, F., Toḿs, S., Bravo-Aranda, J.A., Comerón, A., Rocadenbosch, F., Wagner, F., Pujadas, M., Alados-Arboledas, L., 2012. Monitoring of the Eyjafjallajökull volcanic aerosol plume over

the Iberian Peninsula by means of four EARLINET lidar stations. Atmos. Chem. Phys. 12, 3115–3130. https://doi.org/10.5194/acp-12-3115-2012.

Sicard, M., Rodríguez-Gómez, A., Comerón, A., Muñoz-Porcar, C., 2020. Calculation of the overlap function and associated error of an elastic lidar or a ceilometer: cross-comparison with a cooperative overlap-corrected system. Sensors (Switzerland) 20, 1–9. https://doi.org/10.3390/s20216312.

Stein, A.F., Draxler, R.R., Rolph, G.D., Stunder, B.J.B., Cohen, M.D., Ngan, F., 2015. Noaa's hysplit atmospheric transport and dispersion modeling system. Bull. Am. Meteorol. Soc. 96, 2059–2077. https://doi.org/10.1175/BAMS-D-14-00110.1.

Stewart, C., Damby, D.E., Horwell, C.J., Elias, T., Ilyinskaya, E., Tomašek, I., Longo, B.M., Schmidt, A., Carlsen, H.K., Mason, E., Baxter, P.J., Cronin, S., Witham, C., 2022. Volcanic air pollution and human health: recent advances and future directions. Bull. Volcanol. 84 https://doi.org/10.1007/s00445-021-01513-9.

Titos, G., Ealo, M., Román, R., Cazorla, A., Sola, Y., Dubovik, O., Alastuey, A., Pandolfi, M., 2019. Retrieval of aerosol properties from ceilometer and photometer measurements: long-term evaluation with in situ data and statistical analysis at montsec (southern Pyrenees). Atmos. Meas. Tech. 12, 3255–3267. https://doi.org/10.5194/amt-12-3255-2019.

Toledano, C., Bennouna, Y., Cachorro, V., Ortiz de Galisteo, J.P., Stohl, A., Stebel, K., Kristiansen, N.I., Olmo, F.J., Lyamani, H., Obregón, M.A., Estellés, V., Wagner, F., Baldasano, J.M., González-Castanedo, Y., Clarisse, L., de Frutos, A.M., 2012. Aerosol properties of the Eyjafjallajökull ash derived from sun photometer and satellite observations over the Iberian Peninsula. Atmos. Environ. 48, 22–32. https://doi.org/10.1016/j.atmosenv.2011.09.072.

Veefkind, J.P., Aben, I., McMullan, K., Förster, H., de Vries, J., Otter, G., Claas, J., Eskes, H.J., de Haan, J.F., Kleipool, Q., van Weele, M., Hasekamp, O., Hoogeveen, R., Landgraf, J., Snel, R., Tol, P., Ingmann, P., Voors, R., Kruizinga, B., Vink, R., Visser, H., Levelt, P.F., 2012. TROPOMI on the ESA Sentinel-5 precursor: a GMES mission for global observations of the atmospheric composition for climate, air quality and ozone layer applications. Remote Sens. Environ. 120, 70–83. https://doi.org/10.1016/j.rse.2011.09.027.

Watkin, S.C., 2003. The application of AVHRR data for the detection of volcanic ash in a volcanic ash advisory Centre. Meteorol. Appl. 10, 301–311. https://doi.org/10.1017/S1350482703001063.

Welton, E.J., Campbell, J.R., Spinhirne, J.D., Scott III, V.S., 2001. Global monitoring of clouds and aerosols using a network of micropulse lidar systems. In: Lidar Remote Sensing for Industry and Environment Monitoring, 4153. International Society for Optics and Photonics, pp. 151–158. https://doi.org/10.1117/12.417040.